Sulfate minerals control dissolved rare earth element flux and Nd isotope signature of buoyant hydrothermal plume (EMSO-Azores, 37°N Mid-Atlantic Ridge)

Valérie Chavagnac, Hassan Saleban Ali, Catherine Jeandel, Thomas E Leleu, Christine Destrigneville, Alain Castillo, Laura Cotte, Matthieu Waeles, Cécile Cathalot, Agathe Laës-Huon, et al.

Chemical Geology
November 2018, Volume 499, Pages 111-125
http://dx.doi.org/10.1016/j.chemgeo.2018.09.021
http://archimer.ifremer.fr/doc/00456/56733/

Sulfate minerals control dissolved rare earth element flux and Nd isotope signature of buoyant hydrothermal plume (EMSO-Azores, 37°N Mid-Atlantic Ridge)

Chavagnac Valérie [1, *], Saleban Ali Hassan [1], Jeandel Catherine [2], Leleu Thomas [1], Destrigneville Christine [1], Castillo Alain [1], Cotte Laura [3, 4], Waeles Mathieu [3], Cathalot Cecile [5], Laes Agathe [6], Pelleter Ewan [5], Nonnotte Philippe [7], Sarradin Pierre-Marie [4], Cannat Mathilde [8]

[1] Géosciences Environnement Toulouse, GET, Université de Toulouse, CNRS, IRD, UPS, 14 A Edouard Belin, 31400 Toulouse, France
[2] Laboratoire d'Etudes en Géophysique et Océanographie Spatiales, LEGOS, Université de Toulouse (CNRS, CNES, IRD, UPS), 14 A Edouard Belin, 31400 Toulouse, France
[3] LEMAR CNRS-UMR 6539, IUEM, Université de Bretagne Occidentale, place Copernic, 29280 Plouzané, France
[4] Laboratoire Environnement Profond (LEP/EEP/REM), Ifremer, ZI de la Pointe du Diable, CS 10070, 29280 Plouzané, France
[5] Laboratoire de Cycles Géochimiques (LCG/GM/REM), Ifremer, ZI de la Pointe du Diable, CS 10070, 29280 Plouzané, France
[6] Laboratoire Détection, Capteurs et Mesures (LDCM/RDT), Ifremer, ZI de la Pointe du Diable, CS 10070, 29 280 Plouzané, France
[7] Laboratoire Géosciences Océan, LGO, IUEM, Université de Bretagne Occidentale (CNRS, IRD), place Copernic, 29280 Plouzané, France
[8] Institut de Physique du Globe de Paris, Université Sorbonne Paris Cité (CNRS), 1, rue Jussieu, 75238 Paris Cedex 05, France

* Corresponding author : Valérie Chavagnac, email address : valerie.chavagnac@get.omp.eu

Abstract :

While hydrothermal vents are now thought to be a major source of dissolved iron to the oceans, they have always been considered to be a sink for the dissolved rare-earth elements (DREEs). However, true dissolved REE observations in hydrothermal plumes are still lacking. Here we report for the first time the DREE concentrations and neodymium isotopic compositions (DεNd) of buoyant hydrothermal fluids at Lucky Strike (Mid-Atlantic Ridge). We find that 27 to 62% of total hydrothermal DREEs are rapidly scavenged by anhydrite precipitation at the onset of buoyant plume formation. After this initial loss, all DREEs behave quasi-conservatively within the buoyant plume. Dissolved phase εNd (DεNd) in the evolving plume are identical to black smoker DεNd of +9.0 and contrast radically with DεNd of the local deep water mass at −12.0. Plume DεNd as low as +6.6 may be reconciled by dissolution of newly formed barite in the local environment and carrying seawater DεNd signature. We find, based on the first plume DREE observations, that hydrothermal plumes are in fact a source of DREE to the North Atlantic Deep Water. Precipitation/dissolution processes of hydrothermally-derived minerals, i.e. sulfates in the buoyant plume and Fe oxy-hydroxide in the non-buoyant plume, will likely affect the fate of other

trace metals and their isotopic composition.

Keywords : Black smokers, Rare earth elements, Neodymium isotopes, Hydrothermal, Sulfate minerals, EMSO-Azores

1. Introduction

Hydrothermal submarine vents are known to be a important source for some elements to the oceans (Elderfield and Schultz, 1996). Fluids from hydrothermal fields located at mid-ocean ridges display similar REE patterns when normalized to chondrite or Post-Archean average Australian Sedimentary rocks (PAAS). They show light REEs (LREEs) enrichment over heavy REEs (HREEs), together with positive europium anomalies, and concentration enrichment factors of 10 to 10^3 compared to seawater concentrations (Michard and Albarède, 1986; Michard, 1989; Klinkhammer et al., 1983, 1994; Mitra et al., 1994; Douville et al., 1999; Bau and Dulski, 1999; Schmidt et al., 2010). In comparison, REE patterns of black smoker fluids collected at back-arc basins and subduction zones exhibit either LREEs or MREEs enriched compared to HREEs (Craddock et al., 2010; Cole et al., 2014). The behavior of hydrothermal REEs once expelled into deep seawater has been inferred solely from the REE signatures of suspended particulate matter (SPM) and/or sediment cores in the vicinity of hydrothermal vents (Trocine and Trefry, 1988; German et al., 1990, 1991, 2002; Rudnicki and Elderfield, 1993; Sherrell et al., 1999; Chavagnac et al., 2005, 2006, 2008; German and Seyfried, 2014). Generally, it is thought that hydrothermal systems are sinks for marine DREE due to scavenging onto Fe-bearing minerals in hydrothermal plumes. SPM in the non-buoyant hydrothermal plume is dominated by Fe oxy-hydroxides which are indeed enriched in particle-reactive elements, such as the REEs (German et al., 1990, 1991, 2002; Sherrell et al., 1999). However, high plume DFe levels have been detected in the deep-water column over several hundreds of km away from hydrothermal vents at the ridge axis (Nishioka et al., 2013; Saito et al., 2013; Resing et al., 2015), suggesting that Fe-associated oceanic tracers and more specifically the DREEs might also show similar behavior.

Klar et al. (2017) showed that isotope fraction of dissolved Fe observed in the buoyant hydrothermal plume cannot be reconciled solely by dilution with the background seawater but

reflects the role of Fe-ligand complexation and the presence of labile particulate Fe. A thorough assessment of the dissolved/particulate partitioning in the buoyant plume is therefore needed to better characterize the export of other hydrothermal trace metals (Waeles et al., 2017) and DREEs in the open ocean. Furthermore, recent studies illustrated that the Nd isotopic composition (ε_{Nd}) is a key tracer to quantify Nd (and REE) transfer between particulate and dissolved phases (Lacan and Jeandel, 2001, 2005; Jeandel et al., 2013; Jeandel, 2016). Therefore, measurements of DREEs and Nd isotopic signature in hydrothermal plumes can provide important new information to address the role of hydrothermal systems as a DREE source or sink to the Oceans.

Here, we report on the DREE concentrations and the DNd isotopic compositions of buoyant hydrothermal fluids collected within the first seconds of black smoker fluids mixing with seawater. For the first time, we used an *in-situ* filtration approach which limits chemical exchanges between dissolved and particulate phases (> 0.45µm) during sampling, thus providing a unique opportunity to assess the fate of DREEs along the mixing gradient of hydrothermal fluids by local deep seawater. The Lucky Strike hydrothermal field (LSHF) at 37°N along the Mid Atlantic Ridge (MAR) was chosen because the hydrothermal activity at this location has been monitored continuously since 2010 by the EMSO-Azores deep-sea observatory (Colaço et al., 2011). The considerable contrast in ε_{Nd} between the mid-ocean ridge basalt (i.e. +7 to +10) and the surrounding deep seawater (i.e. -12) is favorable to the detection of any dissolved/particulate exchange processes in the water column.

2. Geological setting and sample collection

2.1. Study area

The Lucky Strike hydrothermal field (LSHF) is located on the MAR at 37°17'N, ˜400km to the Southwest of the Azores archipelago (Fig. 1; Langmuir et al., 1997). The LSHF is

hosted on a basaltic substratum at a depth of ˜1700 meter below sea level on top of a central submarine volcano, where 20 to 30 active vent sites are reported (Langmuir et al., 1997; Von Damm et al., 1998; Charlou et al., 2000; Barreyre et al., 2012; Escartin et al., 2015). The LSHF is surrounded by the North Atlantic Deep Water (NADW; Zheng et al., 2016).

Monitored hot hydrothermal fluids (196-340ºC) show persistent annual inter-site differences in the chloride composition of black smoker fluids, resulting from distinct fluid pathways and distinct rock compositions in the subsurface reaction zone and/or in the upflow zone (Langmuir et al., 1997; Von Damm et al., 1998; Charlou et al., 2000; Pester et al., 2012; Leleu, 2017; Leleu et al., submitted). The distribution of major and trace elements argues for a single source that undergoes phase separation at 2500-2800 meter below the seafloor at a temperature of 430-440°C and feeds the entire LSHF (Leleu et al., submitted). Temperature of the roof of the reaction zone is estimated at 400°C for the Capelinhos vent but clusters around 370°C for the other vents at the LSHF. Salinity differences between sites originate from a permeability gradient within the subsurface, where vapor-dominated fluids preferentially flow through large conduits and fissures while the brine-dominated phase will tend to fill porosity and smaller scale fissures (Leleu et al., submitted; Fontaine et al., 2007). Dissolved Fe and Mn concentrations are 3 to 5 times higher in Capelinhos fluids compared to other LSHF vents and are controlled by processes in the upflow zone, including brine saturation, permeability and faulting (Leleu et al., submitted).

2.2. Sample collection

During two maintenance cruises to EMSO-Azores aboard the R/V *Pourquoi Pas?* in 2014 and 2015, black smoker and buoyant plume fluids were collected back to back during ROV Victor 6000 dives using dedicated fluid samplers at four selected black smokers named Capelinhos, Aisics, White Castle, and Y3 (Table 1). The selected vents cover the entire

chlorinity diversity of the LSHF fluids, i.e. 267 to 574 mM, together with their evolving buoyant hydrothermal plumes. In-situ temperature measurement of black smokers was carried out using the high temperature sensor of the ROV Victor 6000 prior to any fluid sampling. High temperature hydrothermal fluids were sampled by inserting the snorkel of gas-tight titanium syringes into the main chimney, which were triggered via the hydraulic arm of the ROV Victor 6000 (Fig. 2A). At each dive, up to 4 gas-tight titanium syringes were triggered per smoker to determine the composition of the hydrothermal end-member after extrapolation to zero-Mg levels (Table 1). Coupled to the gas-tight syringe sampling, the mixing gradients between black smoker fluid and deep seawater were sampled using the *in-situ* filtration PEPITO sampler deployed on the ROV Victor 6000 (Fig. 2B; Cotte et al., 2015; Waeles et al., 2017). Each sampling was performed by pumping water through a 0.45 µm filter into an acid-cleaned blood-bag using an acid-cleaned titanium-Tygon inlet coupled to the ROV temperature probe (Cotte et al., 2015; Waeles et al., 2017). At each dive, sampling was carried out towards increasing temperatures. The snorkel of the PEPITO sampler was first placed at 1 to 2 m from the vent orifice at temperature ~ 4°C and then shifted downward within the central part of the buoyant plume to take samples every 10°C until reaching 140-150°C (Cotte et al., 2015; Waeles et al., 2017) (Fig. 2B, Table 1).

Immediately after the recovery of the ROV Victor 6000 on board the research vessel, both gas-tight fluid samplers and PEPITO instrument were transferred to a dedicated chemical lab for fluid extraction. First, gases were extracted from gas-tight samplers and transferred into vacuum stainless steel canisters. The fluid samples were then extracted, filtered through 0.45µm Millipore filters and split into different aliquots for aboard and onshore analysis and stored at 4°C in a cold room. pH, Eh, salinity, conductivity, and H_2S were measured on-board immediately after processing. H_2S concentrations were measured in the solution with an amperometric micro-sensor (AquaMS, France). The in-situ filtered PEPITO blood bags

contained between 130 and 2100 mL of buoyant hydrothermal fluids. 3 to 6 samples were selected among the 15 buoyant plume fluids collected at each site, for further DREE and DNd isotope analyses. An aliquot of 125 to 250 ml for each sample was transferred from the *in-situ* filtered bags into acid-cleaned low-density polypropylene bottles, and acidified with 100 to 200 µl of bi-distilled concentrated HCl, prior to storage at 4ºC in a cold room. pH measurements were also carried out on board on the in-situ filtered and un-acidified fluids.

3. Analytical methods

The analytical methods used for major and trace element concentrations in hydrothermal fluid and plume were described in details in previous publications (Besson et al., 2014; Cotte et al., 2015; Leleu, 2017; Waeles et al., 2017).

3.1. Fluid processing for DREE concentration analyses

The REE pre-concentration and purification technique developed for seawater (Tachikawa et al., 1999; Lacan and Jeandel, 2001), had to be modified and adapted to the chemical composition of hydrothermal fluids. Before any chemical treatment, a solution of triple-spikes i.e. ^{146}Nd, ^{153}Eu and ^{174}Yb isotopes, was added to all samples together with a droplet of ultrapure H_2O_2 to ensure the conversion of all dissolved Fe present as Fe^{2+} in reducing hydrothermal fluids, to its oxidized Fe^{3+} form. The pH of the solution was increased to 8 with NH_3-H_2O solution to provoke the precipitation of Fe oxy-hydroxide particles $Fe(OH)_3$ which scavenge all dissolved REEs (Lacan, 2002). The precipitate was rinsed three times with MQ-H_2O to ensure the removal of all major ions, e.g. Na and Ba in particular. Isolation of the REE from the remaining major elements and Fe was carried out using two-step ion exchange columns and elution with ultra-pure bi-distilled acids. REE concentrations were determined with a High-Resolution Inductively Coupled Mass Spectrometer (HR-ICP-MS) Thermofisher

Scientific Element XR at the Observatoire Midi-Pyrénées. Sample introduction was done using an Aridus desolvating nebulizer to reduce oxide formation (<0.05%). Purified REE were re-dissolved in a HNO_3 0.3N solution doped with indium and rhenium to track instrumental drift during sample analysis. Calibration of the instrument was performed with an in-house multiple REE standard at 10, 50 and 100ppt. Measured background intensities of ultraclean HNO_3 0.3N in between samples were subtracted from the sample intensity, which corresponds to 0.01-0.2% for the LREE and 0.2-0.6% for the HREEs. Average Nd blanks are 0.6 ppt, <<< than several ngs of Nd in the sample. Instrumental errors are usually less than 3% for the LREEs and 6% for the HREEs (Tachikawa et al., 1999).

3.2. Nd isotopic compositions

The un-spiked fluid samples were treated through the previous steps of co-precipitation, and double ion exchange columns with an additional step one to isolate Nd from the other REEs. Nd isotopic compositions were measured on a Thermo-Ionization Mass Spectrometer Thermofisher Scientific Triton at the IUEM (European Institut for Marine Studies, Pole Spectrométrie Océan, Brest, France) laboratory in Brest. The $^{143}Nd/^{144}Nd$ ratio was defined as the average of a minimum of 100 measurements of ion intensities following the static multi-collection mode. The $^{143}Nd/^{144}Nd$ ratios were normalized to $^{146}Nd/^{144}Nd = 0.7219$. Measured $^{143}Nd/^{144}Nd$ values for La Jolla standard of 1-5 ng Nd (recommended value of 0.511860) was 0.511850 ± 12 ($1\sigma_E$, n = 13). The Nd isotopic composition uses a ε_{Nd} notation to reflect the $^{143}Nd/^{144}Nd$ ratio compared to CHUR (Chondrite Uniform Reservoir, $^{143}Nd/^{144}Nd$ = 0.512638; Bouvier et al., 2008) on the parts per ten-thousand scale (ε_{Nd} = $(((^{143}Nd/^{144}Nd_{sample}/^{143}Nd/^{144}Nd_{CHUR}) - 1)*10000)$.

3.3. Scanning electron microscopy (SEM) and energy dispersive spectroscopy (EDS)

Mineral analyses and chemical maps were performed on filters sampled in the LSHF buoyant plumes using Scanning electron microscopy (SEM) coupled to Energy Dispersive Spectroscopy (EDS). Investigations were done with a FEI Quanta 200 SEM equipped with an OXFORD Instrument X-MAXN Silicon Drift Detector (detector size: 80mm2) EDS on C-coated fragments of the 0.45 µm filters. Secondary electron images were performed for textural and morphology characterization of the particulate material collected in situ. In addition, X-ray semi-quantitative EDS maps were performed on an area of about 1mm2 and elaborated with the "Large Area Mapping" module of the OXFORD AZtec software. Each area was composed of over 150 fields and each field (130µm*114 µm) was scanned with a resolution of 512*448 pixels (1 pixel = 0.25 µm).

4. RESULTS

4.1. Quantification of hydrothermal end-member contribution to the buoyant hydrothermal plume.

The composition of the end-member hydrothermal fluids is calculated by linear extrapolation to zero-Mg of the least-square regression method applied on fluid data, i.e. fluids collected by gas-tight titanium syringes (Von Damm, 1988). The data are reported in Table 1. The DBa concentration of the end-member hydrothermal fluid is based on the sample exhibiting the lowest DMg concentrations because pure hydrothermal fluids exhibits DMg close to zero. The DBa of hydrothermal fluids decreases at increasing DMg concentration (i.e. dilution by NADW), most likely due to barite precipitation.

The proportion of hydrothermal end-member in the buoyant plume fluids, i.e. the extent of dilution by local seawater, can be determined using two independent parameters: 1) in-situ temperature measurements, i.e. adiabatic mixing hypothesis, and 2) dissolved Mg (or dissolved Mn) concentrations of the solution, i.e. conservative behavior of Mg (or Mn) within

the buoyant hydrothermal plume and hence during the early stages of fluid and seawater mixing, as illustrated in Figure 3A. Apart from two exceptions at Y3 site, all buoyant fluid samples plot within error bars onto the mixing trend, indicating consistent calculated proportions of hydrothermal end-member and NADW sources in the buoyant fluid mixture. Moreover, the proportions found for the black smoker fluids are very close to the calculated end-member, i.e. >97% of hydrothermal end-member. In comparison, the samples of buoyant hydrothermal plume fluids are composed of 14-50% of hydrothermal end-member, corresponding to a dilution factor of 2 - 7.1 by NADW.

4.2. Dissolved REE concentrations

Observed ΣDREE concentrations are shown in Figure 3B and their NADW-normalized REE patterns are illustrated in Figure 4. All hydrothermal plume fluids have ΣDREE concentrations lower than those of their respective end-member fluid but significantly higher than those of NADW (Table 2). The highest ΣDREE values (3.4 – 6.0 nM) are obtained at Aisics while the lowest ones (1-1.5 nM) are measured at Capelinhos. The DREE patterns of buoyant hydrothermal fluids mimic those of hydrothermal end-members, reflecting different degrees of dilution with NADW. Overall, all samples display a strong DLREE over DHREE enrichment with $(La/Yb)_N$ values ranging from 2.3 - 53, and strong positive Eu/Eu* and Ce/Ce* anomalies of 8.1 - 24.7 and 3.6 - 4.4 respectively. Yet, La/La* anomalies display some variability at Aisics for example, where the most diluted fluids of the buoyant plume have positive La/La* anomalies compared to negative La/La* in the least diluted fluids. Note that Capelinhos fluids whether diluted or not by NADW, display concave downward-shaped NADW-normalized DREE patterns, highlighted by DMREE enrichment over DLREE and DHREE.

4.3. Dissolved Nd isotope compositions

The $D\varepsilon_{Nd}$ values of collected hydrothermal fluids vary between +9.0 at Aisics and White Castle and +7.8 at Capelinhos and Y3. In comparison, the $D\varepsilon_{Nd}$ values of buoyant hydrothermal plumes vary between +6.6 and +8.9, the latter being identical within error to the DNd isotope signature of their corresponding black smoker fluids. The dataset is reported in Table 2.

4.4. Particulate phase in the buoyant hydrothermal fluid

Sulfate minerals (anhydrite, gypsum and barite) are present on filters collected within each of the studied LSHF buoyant plumes, with crystals that can be larger than 50µm (Figure 5). On the filter collected within the White Castle buoyant plume at ˜70% mixing of hydrothermal fluid with NADW, large anhydrite crystals (Figure 5A) and very fine Ca-sulfate minerals (<1µm) with a patchy distribution (Figure 5C) covers 2 % of the investigated area (Figure 5C). Barite particles (Figure 5B and 5C) are less abundant at <0.4%.

5. DISCUSSION

5.1. DREE signature of black smoker fluids

At LSHF, black smoker end-member fluids are significantly more enriched in ΣDREEs than NADW, i.e. three orders of magnitude for the DLREEs and one order for the DHREEs. DREE concentrations of LSHF fluids are controlled by three major processes, i.e. brine/vapor phase separation at depth in the vicinity of the magma chamber, physico-chemical properties of the fluid and sub-surface processes linked to secondary mineral formation (Allen and Seyfried, 2005). Under reducing conditions such as those encountered in hydrothermal fluids, DREEs may form strong complexes with anions, among which chloride (Cl) is the main inorganic REE-binding ligand in the hydrothermal fluid. Major and trace element

distributions among the wide range of fluid chlorinity (i.e. 267 - 574 mM) at LSHF are controlled by phase separation of a single deep-rooted fluid (Leleu, 2017). Cl concentrations correlate positively with increasing end-member Nd/Yb ratios while the concentrations of ∑DREEs or each DREE do not. As a result, the effect of phase separation leads to preferential DLREE enrichment in the brine phase while the vapor phase must be relatively enriched in DHREEs, in line with experimental results (Shmulovich et al., 2002). In addition, the positive Eu/Eu* anomalies do not show any trend along the chlorinity and pH range, suggesting that the magnitude of the Eu/Eu* anomalies is independent from phase separation but possibly related either to physical and chemical properties of fluid, alteration of primary plagioclase or shallower sub-surface processes (Haas et al., 1995; Douville et al., 1999; Allen and Seyfried, 2005). In reduced hydrothermal fluids, mobility of Eu in the divalent form is enhanced while that of the other DREEs in the trivalent state is mainly controlled by secondary mineral assemblage (Allen and Seyfried, 2005; Migdisov et al., 2016). As Eu^{2+} and Sr^{2+} have similar ionic radii (Shannon, 1976), Eu can be incorporated into the same secondary minerals. The concave downward-shaped DREE patterns of the Capelinhos fluid are likely related to anhydrite precipitation in agreement with previous anhydrite studies that show preferential uptake of LREE (Mills and Elderfield, 1995; Schmidt et al., 2010; Craddock et al., 2010; Cole et al., 2014).

5.2. DREE signature of buoyant hydrothermal fluids

In the buoyant hydrothermal plume, the SPM are dominated by Fe-bearing sulfide and oxy-hydroxide particles that are efficient scavengers of both hydrothermal fluid and seawater DREE (Mottl and McConachy, 1990; Bau and Dulski, 1999; Field and Sherrell, 2000; Edmonds and German, 2004). Therefore, the fate of hydrothermal DREEs should be closely linked to that of DFe. The DREEs reported here, were acquired on the same fluid samples

analyzed for DFe concentrations whose results are reported in Waeles et al. (2017). These authors showed that 90% of the Fe in the buoyant plume at LSHF remains in the dissolved phase until the plume reaches a dilution factor of 100 with NADW (i.e. 4°C). Furthermore, particles which includes a few µM of Fe (well below the concentration of DFe) are strictly limited to copper- and zinc-bearing sulfides. The measured dissolved Fe/Mn ratios of buoyant hydrothermal fluids are very similar to those of their respective calculated black smoker end-members (see Table 1 and 2). The DFe and DMn behavior suggests that DREEs should be preserved in the dissolved phases in the buoyant plume. Therefore, the plume ΣDREE concentrations exhibit systematically lower values than those expected from the dilution of their respective black smoker end-members - whatever the chloride concentrations (Figure 3B). Comparing the calculated ΣDREE under the hypothesis of their conservative behavior during mixing with the observed data reveals a loss of 7 to 90% (Table 3). Furthermore, the measured DREE concentrations (apart from two exceptions at Aisics and Y3) correlate linearly and positively with the proportion of hydrothermal end-member in the mixture (Figure 3B and Table 3). This suggests that following the initial, abrupt drop in DREE concentrations when the hot fluid discharges into seawater, the DREE behave quasi conservatively as the plume is further diluted by seawater to the temperature ranges of plume sample collection (Figure 6). DREE scavenging by Fe-bearing copper and zinc sulfides may explain the lowest percentage of DREE loss observed (12%), as sulfides are the most common minerals found within one meter of chimney vent discharge (Feely et al., 1990, 1994). However, sulphide precipitation cannot explain as much as 90% DREE loss, due to the low values of the distribution coefficient of REEs in sulfides (Morgan and Wandless, 1980; Mills and Elderfield, 1995). These observations suggest the involvement of a mineral phase which 1) scavenges DREEs, 2) does not require Fe as a major element constituent, and 3) precipitates at the earliest stage of buoyant plume formation.

5.3. Impact of anhydrite precipitation on hydrothermal DREEs distribution

Apart from amorphous silica, anhydrite ($CaSO_4$) and barite ($BaSO_4$) are the most abundantly observed hydrothermal minerals after Fe-bearing sulphides (Feely et al., 1990; Lilley et al., 1995). These minerals are observed on the filter membranes collected through *in-situ* filtration of the buoyant hydrothermal fluids (Figure 5). They exhibit NADW-normalised REE patterns characterized by pronounced LREE enrichments over HREE and positive Eu/Eu* and Ce/Ce* anomalies (Guichard et al., 1979; Barrett et al., 1990; Mills and Elderfield, 1995; Humphris et al., 1998). Their precipitation from hydrothermal fluids will reduce both the dissolved calcium (DCa) and the dissolved Ba (DBa) concentrations and take up preferentially DLREEs over DHREEs. Note that anhydrite is more stable at high temperature (>150ºC) than barite. The geochemical features of the scavenged DREE fraction can be estimated from the differences between the end-member DREE concentrations and those obtained by linear regression of the buoyant plume data at hydrothermal contribution equal to 100%, i.e. DMg equal to zero. This is presented in Figure 6 for the Aisics vent, whereby the difference is noted as Δ notation for each element. We observed that 25 - 30 % of hydrothermal DCa are lost, corresponding to 0.27, 0.88 and 1.5 $g.l^{-1}$ of anhydrite precipitation at Capelinhos, Aisics and White Castle, respectively. This is confirmed by the NADW-normalized DREE concentrations of the missing fraction which show similar features to those of anhydrite found at the TAG hydrothermal mound (Mills and Elderfield, 1995; Humphris et al., 1998) (Table 3 and Figure 7).

The impact of anhydrite precipitation on the distribution of DREEs from hot to buoyant hydrothermal fluids may be assessed based on the distribution coefficient (K_D) of the considered phase (Table 4). The distribution coefficient is defined as:

$$K_D = \frac{REE\ in\ missing\ fraction\ (ppt)}{REE\ in\ end{-}member\ hydrothermal\ fluid\ (ppt)} \qquad \text{Eq(1)}$$

This approach is detailed in Onuma et al. (1966), Guichard et al. (1979) and Morgan and Wandless (1980) and will not be repeated here. The DREEs will substitute major ions in the mineral phase with the closest ionic radius to the individual REE. The logarithm of K_D are plotted against the square of the ionic radii difference between each of the REEs (r_{REE3+}) and the substituted major cation, i.e. Ca^{2+} for anhydrite (r_{Ca2+}), in Figure 8. We took the effective ionic radii of REE^{3+} (apart from Eu^{2+}) and Ca^{2+} reported by Shannon (1976) assuming eightfold coordination number. Note that the coordination number impacts the effective ionic radii of each REE (Shannon, 1976) but not the calculated K_D (Morgan and Wandless, 1980). All calculated K_D of REEs in anhydrite calculated with Eq(1) lie between 10^{-1} and 1 (Table 4), significantly lower values of than 10^3 - 10^4 calculated from anhydrite deposits (Mills and Elderfield, 1995; Cole et al., 2014). This discrepancy is probably due to kinetics effects as anhydrite precipitates instantaneously at the onset of black smoker discharge to surrounding deep seawater, while hydrothermal mounds grows over longer timescales of up to that of metal deposit formation. Meanwhile, for increasing chlorinity values of end-member hydrothermal fluids, the K_D values of REE tend to fall on a linear trend and the K_D value of Eu^{2+} increases in comparison to those of its neighboring REE. These chemical features indicate that chlorinity values of the solution control the distribution of REE between anhydrite and black smoker fluids and the variability of Eu/Eu* anomalies measured on anhydrite at hydrothermal deposits. Alternatively, the K_D values of anhydrite calculated for MREEs (Sm to Dy) at Aisics are very low compared to LREE and HREE obtained from other sites, suggesting that MREE are preferentially partitioned into the fluid phase. This is clearly evidenced by the concave downward-shaped NADW-normalized REE patterns of the most vapor-dominated Capelinhos fluids (Figure 4).

5.4. Impact of sulfate mineral precipitation on $D\varepsilon_{Nd}$ signature of the buoyant plume

DNd isotopic compositions were measured on both black smoker and buoyant plume samples (Table 2). The purest black smoker fluids, i.e. >97% of hydrothermal end-member, display variable $D\varepsilon_{Nd}$ of +9.0 for Aisics and White Castle and +7.8 for Y3 and Capelinhos. There is no correlation between black smoker $D\varepsilon_{Nd}$ values and Cl content. These values reflect the Nd isotope signature of the basaltic substratum at LSHF which vary mainly between +7.0 and +9.4 (Hamelin et al., 2013). These results provide clear evidence that the $D\varepsilon_{Nd}$ signature of hydrothermal fluids records and preserves the ε_{Nd} of their substratum. The $D\varepsilon_{Nd}$ values of the buoyant plume fluids are either identical to or lower by up to 2.4 $D\varepsilon_{Nd}$ units than those of their respective hydrothermal black smoker fluids, i.e. +8.9 to +6.6 at 14-50% contribution of hydrothermal end-member in the plume mixture (Figure 9). These shifts in $D\varepsilon_{Nd}$ are significant and suggest the incorporation of Nd and other DREE from the admixing NADW with ε_{Nd} of -12. These significantly lower $D\varepsilon_{Nd}$ values of the buoyant hydrothermal fluids could result from two different mechanisms.

1) At the onset of buoyant plume formation, anhydrite precipitation may scavenge 27, 53, 55 and 37% of hydrothermal DNd at Aisics, White Castle, Capelinhos and Y3 respectively (Table 3). If we assume in the conservative mixing equations 1) this initial DNd loss for the black smoker source and 2) the conservative behavior of the hydrothermal DREEs evidenced along the mixing gradient, then the calculated $D\varepsilon_{Nd}$ values of buoyant plume fluids are consistent with the measured ones. For example, two buoyant fluids (PL5-601-C3 et PL5-601-D1, White Castle) exhibit excellent consistency in their DREE concentrations and $D\varepsilon_{Nd}$ results at +8.2, for similar mixing contributions of NADW and black smoker (Figure 9). However, $D\varepsilon_{Nd}$ values as low as +6.6 (Aisics site) require an initial hydrothermal DNd loss of 80 to 90% rather than 27%, which is not observed from DNd concentrations.

2) An alternative (possibly in addition to anhydrite precipitation) mechanism may reside in the occurrence of a specific mineral that may be entrained into the turbulent and vigorous mixing of hydrothermal fluid with local NADW. Its dissolution within the buoyant plume may provide not only an additional source of major cation and Nd but also alter the DNd isotopic signature of the mixture. The size of this mineral should necessarily be smaller than <0.45µm as all analyzed buoyant fluids were filtered *in-situ*. Sulfide minerals such as chalcopyrite, pyrite and sphalerite, exhibit mineral sizes as low as 0.1 µm at the onset of buoyant plume formation (< 1m) (Feely et al., 1990) but their dissolution rates are very slow, i.e. below 5.1 10^{-11} $cm.s^{-1}$ (Feely et al., 1987), precluding their involvement. In contrast, sulfate minerals (barite and anhydrite), present on our buoyant plume filters (Figure 5), show decreasing mineral size with increasing height above the vent discharge. Both sulfate minerals have much faster dissolution rates than sulfides (Feely et al., 1987). The smallest sulfate minerals formed in the NADW-dominated portion of the buoyant hydrothermal plume record the Nd isotopic composition of the surrounding water which is dominated by the $D\varepsilon_{Nd}$ value of NADW at -12. Their partial dissolution will increase DCa and/or DBa concentrations of buoyant hydrothermal fluids, and may evolve the DNd isotopic composition of the buoyant hydrothermal fluids towards $D\varepsilon_{Nd}$ values lower than black smoker $D\varepsilon_{Nd}$. In case of crystal sizes smaller than 0.45 µm, sulfate minerals present in solution might have been dissolved by chemical treatment for sample conditioning, as all buoyant hydrothermal fluids were acidified on-board. Barite dissolution is potentially evidenced by higher DBa concentrations in the buoyant hydrothermal fluids than hydrothermal end-members (Figure 6), arguing for a contribution of 11, 12, 6 and 2 $\mu g.l^{-1}$ of dissolved barite at Aisics, White Castle, Y3 and Capelinhos respectively. With 0.2 $\mu g.g^{-1}$ of Nd for barite (Hein et al., 2007), barite dissolution

supplies ˜3 to 14 pM of DNd to buoyant hydrothermal plumes at LSHF, which is undetectable from DNd concentration measurements (instrumental errors of 3% for LREE), yet observable in the DNd isotopic compositions.

6. IMPLICATIONS

Within the marine environment, different modes of formation of barite have been proposed. First, degradation of organic matter may release substantial amounts of DBa to seawater, creating favorable conditions for barite formation (Griffith and Paytan, 2012). In addition, biological and microbiological studies show the occurrence of small barite crystals formed by bacteria onto the outer shells of mollusks as a result of Ba purging into the extrapallial fluid (Fritz et al., 1990; Gonzalez-Muñoz et al., 2012). At hydrothermal vents and in particular at LSHF, numerous mussel beds flourish around vent discharges taking advantage of organic matter produced by chemolithotrophic bacteria. Caillac et al. (2013) identified nano-crystals of barite associated with organic matter on alteration surfaces of basaltic glasses at a deep-sea hydrothermal vent. A combination of basalt alteration, mollusk proliferation and organic matter availability at LSHF provides an ideal environment for the formation of barite nano-crystals. But up to date, no geochemical and Nd isotopic studies were carried out on such barite bio-mineralization to support or reject this hypothesis.

Alternatively, at the eastern equatorial Pacific, Martin et al. (1995) examined barite minerals present in deep-sea sediments collected underneath the hydrothermal plume trajectory identified by Lupton and Craig (1981) and more recently Resing et al. (2015). The strontium (Sr) and Nd isotope signatures of barite minerals contrast radically with those of foraminifera and fish teeth which record the Sr and Nd isotopic signatures of local seawater, i.e. 0.709160 and ε_{Nd} at -6, respectively. A contribution of hydrothermally-derived barite, even though relatively far from the ridge axis, was proposed to explain least radiogenic Sr

isotopic signature compared to seawater value. However, the systematic unradiogenic barite ε_{Nd}, as lows as -11.8, cannot be reconciled neither with Pacific seawater (ε_{Nd} -6) nor hydrothermal (ε_{Nd} >+6) contributions. Martin et al. (1995) suggested a contribution from an unobserved aeolian input characterized by high Nd concentration and unradiogenic Nd isotopic composition.

While these studies do not necessarily imply that the least radiogenic ε_{Nd} values observed in LSHF buoyant plume samples are influenced by barite, they raise questions on the Nd isotope signature of barite formed via different pathways at hydrothermal vents. Thus far, little is known about barite chemical and isotopic signatures along the continuum from the proximal buoyant plume to the non-buoyant plume within the water column.

7. CONCLUSIONS

The distribution of hydrothermal DREEs and DNd isotope signatures in hydrothermal fluids shed light on the effect of sulfate minerals along the mixing gradient of pure black smoker until its 10-fold dilution by NADW. The four LSHF black smoker fluids record and preserve the DNd isotope signatures of the substratum, i.e. $D\varepsilon_{Nd}$ at +7.8 to +9.0, and exhibit a narrow range of DNd/DFe ratios at $0.4\ 10^{-6}$ - $5.2\ 10^{-6}$. Once expelled into the deep seawater, hydrothermally-derived DREEs are strongly influenced and altered by sulfate minerals: at the onset of buoyant plume formation by anhydrite then by the barite precipitation/dissolution cycle in the buoyant plume. Anhydrite precipitation leads to 27 to 55% scavenging of the hydrothermal DNd budget. After this initial loss, all DREEs behave quasi-conservatively within the buoyant plume and 90% of iron is preserved in the dissolved phase. The imprint of barite is suspected from higher DBa concentrations in the buoyant hydrothermal fluids than hydrothermal end-members together with the $D\varepsilon_{Nd}$ values of buoyant plume fluids which showed a decrease from the black smoker $D\varepsilon_{Nd}$ of +9.0 down to +6.6 in the plume. We find,

based on the first plume DREE observations at LSHF, that hydrothermal plumes are a source of DREE to the NADW. Precipitation and dissolution of sulfate minerals in buoyant plume control the hydrothermal DREE flux to the ocean and alter the Nd isotope signature of local deep seawater while the Fe oxy-hydroxides minerals which dominates the SPM of non-buoyant plume are efficient scavengers of marine DREE budget and record the Nd isotope signature of the surrounding seawater.

Acknowledgements

We thank the captains and crew of the R. *Pourquoi Pas?* and the ROV Victor6000 team for their assistance during sample collection at sea. We acknowledge financial support from the French ANR LuckyScales project (ANR-14-CE02-0008) and the EU EMSO project (http://www.emso-eu.org). This manuscript benefited from the comments of Jeroen Sonke. We acknowledge the comments of two anonymous reviewers and Catherine Chauvel which improved the quality of the manuscript.

Author Contributions Statement

V.C. and C.J. conceived the study. During oceanographic cruises, V.C., T.L. and A.C. collected and processed all high temperature hydrothermal fluids while L.C., C.C., A.L-H. and P.-M.S. collected and processed all buoyant hydrothermal fluids. H.S.A. and T.L. performed the analytical protocols for data acquisition. H.S.A, C.J., V.C. and P.N. carried out the Nd isotopic measurements. C.C. and E.P. carried out the mineralogical study. P.M.S. and M.C. are coordinating the EMSO-Azores program. All authors contributed to the preparation of the manuscript. There is no conflict of interest.

References

Allen, D.E., Seyfried, W.E., 2005. REE controls in ultramafic hosted MOR hydrothermal systems: An experimental study at elevated temperature and pressure. Geochim. Cosmochim. Acta 69, 675–683.

Barrett, T.J., Jarvis, I., Jarvis, K.E., 1990. Rare earth element geochemistry of massive sulfides-sulfates and gossans on the Southern Explorer Ridge. Geology 18, 583-586.

Barreyre, T., Escartín, J., Garcia, R., Cannat, M., Mittelstaedt, E., Prados, R., 2012. Structure, temporal evolution, and heat flux estimates from the Lucky Strike deep-sea hydrothermal field derived from seafloor image mosaics: hydrothermal outflow and image mosaics. Geochem. Geophys. Geosyst. 13, doi: 10.1029/2011GC003990.

Bau, M., Dulski, P., 1999. Comparing yttrium and rare earths in hydrothermal fluids from the Mid-Atlantic Ridge: implications for Y and REE behavior during near-vent mixing and for the Y/Ho ratio of Proterozoic seawater. Chem. Geol. 155, 77-90.

Besson, P., Degboe, J., Berge, B., Chavagnac, V., Fabre, S., Berger, G., 2014. Ca, Na, K and Mg Concentrations in Seawater by Inductively Coupled Plasma Atomic Emission Spectrometry Analyses: Applications to IAPSO Standard Seawater, Hydrothermal Fluids and Synthetic Seawater Solutions. Geostand. Geoanal. Res. 38, 355-362.

Bouvier, A., Vervoort, J.D., Patchett P.J., 2008. The Lu-Hf and Sm-Nd isotopic composition of CHUR : Constraints from unequilibrated chondrites and implications for the bulk composition of terrestrial planets. Earth Planet. Sci. Lett., 273, 48-57, doi.org/10.1016/j.epsl.2008.06.010.

Caillac, N., Rommevaux-Jestin, C., Rouxel, O., Lesongeur, F., Liorzou C., Bollinger, C., Ferrant, A., Godfroy, A., 2013. Microbial colonization of basaltic glasses in hydrothermal organic-rich sediments at Guaymas Basin. Frontiers Microbio. 4, doi: 10.3389/fmicb.2013.00250.

Charlou, J.L., Donval, J.P., Douville, E., Jean-Baptiste, P., Radford-Knoery, J., Fouquet, Y., Dapoigny, A., Stievenard, M., 2000. Compared geochemical signatures and the evolution of Menez Gwen (37°50'N) and Lucky Strike (37°17'N) hydrothermal fluids, south of the azores Triple Junction on the Mid-Atlantic Ridge. Chem. Geol. 171, 49–75.

Chavagnac, V., German, C.R., Milton J.A., Palmer, M.R., 2005. Source of REE in sediments cores from the Rainbow vent site (36°14'N, MAR). Chem. Geol. 216, 329-352.

Chavagnac, V., Palmer, M.R., Milton, J.A., Green, D.R.H., German, C.R., 2006. Hydrothermal sediments as a potential record of seawater Nd isotopic compositions: The Rainbow vent site (36˚14'N, MAR). Paleocean. 21, doi: 10.1029/2006PA001273.

Chavagnac, V., German, C.R., Taylor, R.N., 2008. Global environmental effects of large volcanic eruptions on ocean chemistry: evidence from « hydrothermal » sediments (ODP Leg 185, Site 1149). J. Geophys. Res. 113, doi: 10.1029/2007JB005333.

Colaço, A., Blandin, J., Cannat, M., Carval, T., Chavagnac, , Connelly, D., Fabian, M., Ghiron, S., Goslin, J., Miranda, J. M., Reverdin, G., Sarrazin, J., Waldmann, C., Sarradin P-M., 2011. MoMAR-D: a technological challenge to monitor the dynamics of the Lucky Strike vent ecosystem. ICES J. Mar. Sci. 68, doi: 10.1093/icesjms/fsq075.

Cole, C.S., James, R.H., Connelly, D.P., Hathorne, E.C., 2014. Rare earth elements as indicators of hydrothermal processes within the East Scotia subduction zone system. Geochim. Cosmochim. Acta 140, 20–38.

Cotte, L., Waeles, M., Pernet-Coudrier, B., Sarradin, P.-M., Cathalot, C., Riso, R.D., 2015. A comparison of in situ vs. ex situ filtration methods on the assessment of dissolved and particulate metals at hydrothermal vents. Deep Sea Res. 105, 186–194.

Craddock, P.R., Bach, W., Seewald, J.S., Rouxel, O.J., Reeves, E., Tivey, M.K., 2010. Rare earth element abundances in hydrothermal fluids from the Manus Basin, Papua New

Guinea: Indicators of sub-seafloor hydrothermal processes in back-arc basins. Geochim. Cosmochim. Acta 74, 5494–5513.

Douville, E., Bienvenu, P., Charlou, J.L., Donval, J.P., Fouquet, Y., Appriou, P., Gamo, T., 1999. Yttrium and rare earth elements in fluids from various deep-sea hydrothermal systems. Geochim. Cosmochim. Acta 63, 627–643.

Edmonds, H.N., German, C.R., 2004. Particle geochemistry in the Rainbow hydrothermal plume, Mid-Atlantic Ridge. Geochim. Cosmochim. Acta 68, 759-772.

Elderfield, H., 1988. The oceanic chemistry of the rare-earth elements. Phil. Trans. Royal Soc. London A 325, 105-126.

Elderfield, H., Schultz, A., 1996. Mid-ocean ridge hydrothermal fluxes and the chemical composition of the ocean. Ann. Rev. Earth Planet. Sci. 24, 191–224.

Escartin, J., Barreyre, T., Cannat, M., Garcia, R., Gracias, N., Deschamps, A., Salocchi, A., Sarradin, P.-M., Ballu, V., 2015. Hydrothermal activity along the slow-spreading Lucky Strike ridge segment (Mid-Atlantic Ridge): Distribution, heat flux, and geological controls. Earth Planet. Sci. Lett. 431, 173–185.

Feely, R.A., Geiselman, T.L., Baker, E.T., Massoth, G.J., 1990. Distribution and composition of hydrothermal plume particles from the ASHES vent field at Axial Volcano, Juan de Fuca ridge. J. Geophys. Res. 95, 12855-12873.

Feely, R.A., Massoth, G.J., Trefry, J.H., Baker, E.T., Paulson, A.J., Lebon, G.T., 1994. Composition and sedimentation of hydrothermal plume particles from North Cleft segment, Juan de Fuca ridge. J. Geophys. Res. 99, 4985-5006.

Feely, R.A., Lewison, M., Massoth, G.J., Robert-Baldo, G., Lavelle, J.W., Byrne, R.H., Von Damm, K.L., Curl Jr, H.C., 1987. Composition and dissolution of black smoker particulates from active vents on the Juan de Fuca ridge. J. Geophys. Res. 92, 11347-11363.

Fontaine, F.J., Wilcock, W.S.D., Butterfield, D.A., 2007. Physical controls on the salinity of mid-ocean ridge hydrothermal vent fluids. Earth Planet. Sci. Lett. 257, 132–145.

Field, M.P., Sherrell, R.M., 2000. Dissolved and particulate Fe in a hydrothermal plume at 9°45′N, East Pacific Rise: Slow Fe (II) oxidation kinetics in Pacific plumes. Geochim. Cosmochim. Acta 64, 619–628.

Fritz, L.W., Ragone, L.M., Lutz, R.A., Swapp, S., 1990. Biomineralization of barite in the shell of the freshwater Asiatic clam Corbicula fluminea (Mollusca: Bivalvia). Limnol. Ocean, 35, 756-762.

German, C.R., Klinkhammer, G.P., Edmond, J.M., Mitra, A., Elderfield, H., 1990. Hydrothermal scavenging of rare-earth elements in ocean. Nature 345, 516-518.

German, C.R., Campbell, A.C., Edmond, J.M., 1991. Hydrothermal scavenging at the Mid-Atlantic Ridge: modification of trace element dissolved fluxes. Earth Planet. Sci. Lett. 107, 101–114.

German, C.R., Colley, S., Palmer, M.R., Khripounoff, A., Klinkhammer, G.P., 2002. Hydrothermal plume-particle fluxes at 13°N on the East Pacific Rise. Deep Sea Res. 49, 1921–1940.

German, C.R., Seyfried, W.E., 2014. Hydrothermal Processes. Treatise on Geochemistry 2nd Edition, Elsevier 8, 191–233, doi: 10.1016/B978-0-08-095975-7.00607-0.

Gonzalez-Muñoz, M.T., Martinez-Ruiz, F., Morcillo, F., Martin-Ramos, J.D., Paytan, A., 2012. Precipitation of barite by marine bacteria: A possible mechanism for marine barite formation. Geology 40, 675-678.

Griffith, E.M., Paytan, A., 2012. Barite in the ocean - occurrence, geochemistry and paleoceanographic applications. Sedim. doi: 10.1111/j.1365-3091.2012.01327.x.

Guichard, F., Church, T.M., Treuil, M., Jaffrezic, H., 1979. Rare earths in barites: distribution and effects on aqueous partitioning. Geochim. Cosmochim. Acta 43, 983-997.

Hamelin, C., Bezos, A., Dosso, L., Escartin, J., Cannat, M., Mevel, C., 2013. Atypically depleted upper mantle component revealed by Hf isotopes at Lucky Strike segment. Chem. Geol. 341, 128–139.

Haas, J.R., Shock, E.L., Sassani, D.C., 1995. Rare Earth Elements in hydrothermal systems: Estimates of standard partial molal thermodynamic properties of aqueous complexes of the rare-earth elements at high pressures and temperatures. Geochim. Cosmochim. Acta 59,4329–4350.

Hein, J.R., Zierenberg, R.A., Maynard, J.B., Hannington, M.D., 2007. Barite-forming environments along a rifted margin, Southern California Borderland. Deep-Sea Res. II 54, 1327-1349.

Humphris, S.E., Alt, J.C., Teagle, D.A., Honnorez, J.J., 1998. Geochemical changes during hydrothermal alteration of basement in the stockwork beneath the active TAG hydrothermal mound. Proceed. Ocean Drill. Prog. Sci. Res. 158, 255–276.

Jeandel, C., 2016. Overview of the mechanisms that could explain the « boundary Exchange » at the land-ocean contact. Phil. Trans. Royal Soc. London A 374, doi: 10.1098/rsta.2015.0287.

Jeandel, C., Delattre, H., Grenier, M., Pradoux, C., Lacan, F., 2013. Rare earth element concentrations and Nd isotopes in the Southeast Pacific Ocean: REE and Nd isotopes in the South East Pacific. Geochem. Geophys. Geosyst. 14, 328–341.

Klar, J.K., James R.H., Gibbs, D., Lough, A., Parkinson, I., Milton, J.A., Hawkes, J.A., Connelly, D.P., 2017. Isotopic signature of dissolved iron delivered to the Southern Ocean from hydrothermal vents in the East Scotia Sea. Geology 45, 351-354.

Klinkhammer, G.P., Elderfield, H., Hudson, A., 1983. Rare earth elements in seawater near hydrothermal vents. Nature 305, 185-188.

Klinkhammer, G.P., Elderfield, H., Edmond, J.M., Mitra, A., 1994. Geochemical implications of rare earth element patterns in hydrothermal fluids from mid-ocean ridges. Geochim. Cosmochim. Acta 58, 5105–5113.

Lacan, F., 2002. Masses d'eau des mers Nordiques et de l'Atlantique subarctique traces par les isotopes du Néodyme. Ph.D. Thesis. Université Toulouse III - Paul Sabatier, pp293.

Lacan, F., Jeandel, C., 2001. Tracing Papua New Guinea imprint on the central Equatorial Pacific Ocean using neodymium isotopic compositions and Rare Earth Element patterns. Earth Planet. Sci. Lett. 186, 497–512.

Lacan, F., Jeandel, C., 2005. Neodymium isotopes as a new tool for quantifying exchange fluxes at the continent–ocean interface. Earth Planet. Sci. Lett. 232, 245–257.

Langmuir, C., Humphris, S.E., Fornari, D.J., Van Dover, C., Von Damm, K.L., Tivey, M.K., Colodner, D., Charlou, J.L., Desonie, D., Wilson, C., Fouquet, Y., Klinkhammer, G.P., Bougault, H., 1997. Hydrothermal vents near a mantle hot spot: The Lucky Strike vent field at 37°N on the Mid-Atlantic Ridge. Earth Planet. Sci. Lett. 148, 69–91.

Leleu, T., Chavagnac, V., Cannat, M., Fontaine, F., Ceuleneer, G., and Castillo, A., 2018. Spatial variations in chemistry at the Lucky Strike hydrothermal field, Mid Atlantic Ridge: clues to fluid-rock reactions and fluid pathways in the upflow zone. Submitted to G-Cubed.

Leleu, T., 2017. Variabilité spatio-temporelle de la composition des fluides hydrothermaux (Observatoire Fond de Mer EMSO-Açores, Lucky Strike): Traçage de la circulation hydrothermale et quantification des flux chimiques associés. *Ph.D. Thesis*, University of Toulouse III, 286pp.

Lilley, M.D., Feely, R.A., Trefry, J.H., 1995. Chemical and Biochemical Transformations in Hydrothermal Plumes. In Seafloor Hydrothermal Systems: Physical, Chemical, Biological, and Geological Interactions, Am. Geophys. Union. 369–391.

Lupton, J.E., Craig, H., 1981. A Major Helium-3 Source at 15°S on the East Pacific Rise. Science 214, 13-18, doi: 10.1126/science.214.4516.13.

Martin, E.E., Macdougall, J.D., Herbert, T.D., Paytan, A., Kastner, M., 1995. Strontium and neodymium isotopic analyses of marine barite separates. Geochim. Cosmochim. Acta 59, 1353-1361.

Michard, A., 1989. Rare earth element systematics in hydrothermal fluids. Geochim. Cosmochim. Acta 53, 745–750.

Michard, A., Albarède, F., 1986. The REE content of some hydrothermal fluids. Chem. Geol. 55, 61-60.

Migdisov, A., Williams-Jones, A.E., Brugger, J., Caporuscio, F.A., 2016. Hydrothermal transport, deposition, and fractionation of the REE: Experimental data and thermodynamic calculations. Chem. Geol. 439, 13–42.

Mills, R.A., Elderfield, H., 1995. Rare earth element geochemistry of hydrothermal deposits from the active TAG mound, 26ºN Mid-Atlantic Ridge. Geochim. Cosmochim. Acta 59, 3511-3524.

Mitra, A., Elderfield, H., Greaves, M.J., 1994. Rare earth elements in submarine hydrothermal fluids and plumes from the Mid-Atlantic Ridge. Mar. Chem. 46, 217–235.

Morgan, J.W., Wandless, G.A., 1980. Rare earth element distribution in some hydrothermal minerals: evidence for crystallographic control. Geochim. Cosmochim. Acta 44, 973-980.

Mottl, M.J., McConachy, T.F., 1990. Chemical processes in buoyant hydrothermal plumes on the East Pacific Rise near 21ºN. Geochim. Cosmochim. Acta 54, 1911–1927.

Nishioka, J., Nakatsuka, T., Watanabe, Y.W., Yasuda, I., Kuma, K., Ogawa, H., Ebuchi, N., Scherbinin, A., Volkov, Y.N., Shiraiwa, T., Wakatsuchi, M., 2013. Intensive mixing along an island chain controls oceanic biogeochemical cycles: mixing controls biogeochemical cycles. Global Biogeochem. Cycles 27, 920–929.

Onuma, N., Higuchi, H., Wakati, H., Nagasawa, H., 1966. Trace element partition between two pyroxenes and the host lava. Earth Planet. Sci. Lett. 5, 47-51.

Pester, N.J., Reeves, E.P., Rough, M.E., Ding, K., Seewald, J.S., Seyfried, W.E., 2012. Subseafloor phase equilibria in high-temperature hydrothermal fluids of the Lucky Strike Seamount (Mid-Atlantic Ridge, 37°17′N). Geochim. Cosmochim. Acta 90, 303–322.

Resing, J.A., Sedwick, P.N., German, C.R., Jenkins, W.J., Moffett, J.W., Sohst, B.M., Tagliabue, A., 2015. Basin-scale transport of hydrothermal dissolved metals across the South Pacific Ocean. Nature 523, 200–203.

Rudnicki, M.D., Elderfield, H., 1993. A chemical model of the buoyant and neutrally buoyant plume above the TAG vent field, 26 degrees N, Mid-Atlantic Ridge. Geochim. Cosmochim. Acta 57, 2939–2957.

Saito, M.A., Noble, A.E., Tagliabue, A., Goepfert, T.J., Lamborg, C.H., Jenkins, W.J., 2013. Slow-spreading submarine ridges in the South Atlantic as a significant oceanic iron source. Nature Geoscience 6, 775–779.

Schmidt, K., Garbe-Schönberg, D., Bau, M., Koschinsky, A., 2010. Rare earth element distribution in 400°C hot hydrothermal fluids from 5°S, MAR: The role of anhydrite in controlling highly variable distribution patterns. Geochim. Cosmochim. Acta 74, 4058–4077.

Shannon, R.T., 1976. Revised effective ionic radii and systematic studies of interatomic distances in halides and chalcogenides. Acta Crystal. A 32, 751–767.

Sherrell, R.M., Field, M.P., Ravizza, G.P., 1999. Uptake and fractionation of rare earth elements on hydrothermal plume particles at 9°45′ N, East Pacific Rise. Geochim. Cosmochim. Acta 63, 1709–1722.

Shmulovich, K., Heinrich, W., Möller, P., Dulski, P., 2002. Experimental determination of REE fractionation between liquid and vapour in the systems NaCl–H_2O and $CaCl_2$–H_2O up to 450 °C. Contrib. Mineral. Petrol. 144, 257–273.

Tachikawa, K., Jeandel, C., Roy-Barman, M., 1999. A new approach to Nd residence time: The role of atmospheric inputs. Earth Planet. Sci. Lett. 170, 433–446.

Trocine, R.P., Trefry, J.H., 1988. Distribution and chemistry of suspended particles from an active hydrothermal site on the Mid-Atlantic Ridge at 26ºN. Earth Planet. Sci. Lett. 88, 1-15.

Von Damm, K.L., 1988. Systematics and postulated controls on submarine hydrothermal solution chemistry. J. Geophys. Res. 93, 4551–4561.

Von Damm, K.L., Bray, A.M., Buttermore, L.G., Oosting, S.E., 1998. The geochemical controls on vent fluids from the Lucky Strike vent field, Mid-Atlantic Ridge. Earth Planet. Sci. Lett. 160, 521–536.

Waeles, M., Cotte, L., Pernet-Coudrier, B., Chavagnac, V., Cathalot, C., Leleu, T., Laes-Huon, A., Perhirin, A., Riso, R.D., Sarradin, P.-M., 2017. On the early fate of hydrothermal iron at deep-sea vents: a reassessment after in-situ filtration. Geophys. Res. Lett. 44, doi: 10.1002/2017GL073315.

Zheng, X.-Y., Plancherel, Y., Saito, M.A., Scott, P.M., Henderson, G.M., 2016. Rare earth elements (REEs) in the tropical South Atlantic and quantitative deconvolution of their non-conservative behavior. Geochim. Cosmochim. Acta 177, 217–237.

Figure captions

Figure 1: Location of the Lucky Strike hydrothermal field on the Mid-Atlantic Ridge. Hydrothermal vents are reported on the bathymetric map of the vent field as black stars, among which four active vents (red star) have been sampled for pure and buoyant hydrothermal fluids (Table 1).

Figure 2: Deep-sea photographs of fluid collection at the Aisics hydrothermal vent using titanium gas-tight syringe for black smokers in (A) and the in-situ filtration PEPITO instrument for the buoyant hydrothermal plume in (B) (ROV Victor 6000; IFREMER/CNRS). Locations of fluid collection is represented by blue diamond for buoyant hydrothermal plume.

Figure 3: (A) Calculated percentages of hydrothermal fluid contribution in the collected fluid samples based on in-situ temperature and Mg concentrations, illustrating good correlation between physical and chemical parameters. The line represents the evolution of % hydrothermal fluid in solution during dilution by seawater using binary mixing for conservative Mg and adiabatic mixing equation for temperature. (B) Distribution of the ΣDREEs concentrations as a function of hydrothermal contribution in the collected fluid samples. The dashed lines represent the conservative mixing trends of different hydrothermal end-member fluids diluted by seawater (NADW; Zheng et al., 2016).

Figure 4: NADW-normalized DREE patterns of hydrothermal end-member fluids (in red) and buoyant hydrothermal plumes samples (in blue) at four hydrothermal vents of the Lucky Strike hydrothermal field: Aisics in (A), Y3 in (B), Capelinhos in (C) and White Castle in (D). DREE concentrations of the NADW are from Zheng et al. (2016).

Figure 5: A. Secondary electron (SE) micrograph of a large anhydrite crystal with dissolution texture corresponding to entrained particles into the turbulent proximal plume (White Castle; PL5-601-B1). B. SE micrograph of barite crystals collected within the buoyant plume (White Castle; PL5-601-B1). C. Mosaic SE image and Ba and Ca X-ray maps of the filter collected

within the White Castle buoyant plume (White Castle; PL5-601-B1); Ca X-ray map shows the two types of Ca-sulfates (i.e. large anhydrite grains and very small Ca-sulfates that occurs as patchy zones) which represents around 2% of filter surface.

Figure 6: Concentrations of dissolved Calcium (DCa), Neodymium (DNd) and Barium (DBa) reported as a function of dissolved Magnesium (DMg) for collected black smoker and buoyant hydrothermal plume fluids in A, B and C, respectively at the Aisics vent. The missing fraction noted as ΔDCa, ΔDNd and ΔDNd are indicated. See text for further information. Element concentrations of high temperature hydrothermal fluids are reported in blue while those of buoyant black smoker fluids are in orange.

Figure 7: NADW-normalized REE patterns of the missing REE fractions at each site, in comparison with anhydrite (Humphris et al., 1998), Fe-bearing oxy-hydroxide collected in neutrally buoyant plume by a Stand Alone Pumping System (SAPS) (Edmonds and German, 2004), amorphous silica and barite (Barrett et al., 1990) expected at deep-sea hydrothermal vents.

Figure 8: K_D of REEs for the four missing fractions plotted against $(r_{REE} - r_{Ca2+})^2$.

Figure 9: Variation of plume $D\varepsilon_{Nd}$ signatures for different percentage contributions of hydrothermal end-member in the mixture. These trends are based on conservative mixing equations (black line). The dashed lines mimic a conservative mixing between NADW and hydrothermal end-members which have lost 50, 60, 80 and 90% of their primary hydrothermal DNd concentrations by scavenging. These trends are reported for two hydrothermal buoyant plumes, i.e. Aisics in (A) and White Castle in (B). The black dots represent the observed $D\varepsilon_{Nd}$ signatures at the calculated percentage contribution of hydrothermal end-member in the mixture.

Tables

Table 1: Chemical composition of high temperature and buoyant hydrothermal fluids collected at four active vents of the LSHF. Sampling device for each sample is also mentioned. Temperature values are measured in-situ using high temperature probes of the ROV Victor 6000. The chemical composition of the missing fraction represents the difference between end-member hydrothermal fluids and those obtained by linear regression of the buoyant plume data at hydrothermal contribution equal to 100%, i.e. DMg equal to zero. We indicate the contribution percentage of hot hydrothermal fluid in each of buoyant plume samples based on temperature and DMg concentrations (§: Waeles et al., 2017).

Table 2: Dissolved REE concentrations (in pM) of four selected hydrothermal vents. Nd isotope compositions are also reported for eight buoyant hydrothermal plume fluids and four high temperature hydrothermal fluids. End-member compositions were estimated by extrapolation of all fluids composition concentrations versus DMg relationships to a zero DMg content, as expected in pure hydrothermal end-member. n.m.: not measured; n.d.: not determined. N : NADW (Zheng et al., 2016). $Eu/Eu^* = (2*Eu_N) / (Sm_N + Gd_N)$; $Ce/Ce^* = Ce_N / ((2*Pr_N) - Nd_N)$; $La/La^* = La_N / ((3*Pr_N) - (2*Nd_N))$; $(La/Yb)_N = La_N / Yb_N$.

Table 3: Calculated DREE concentrations of the missing REE fraction.

Table 4: Distribution coefficient (K_D) of REE in anhydrite.

Table 1

Site	Latitude N	Longitude W	depth mbsl	year	Sample name	Sampling device	T in-situ °C	pH	DCl mM	DMg mM	DMn µM§	DFe µM§	DH2S mM§	DCa mM	DBa µM	End-member based on DMg	End-member based on T°C
NADW#							4	8.1	545	54.1	0	0	0	10.28	0.13		
Aisics	37°17.3396	32°16.5357	1689	2015	Pl2-598-D2	PEPITO	97±16	4.97	n.m.	37.67	64	146	0.23	16.57	19.01	30.40%	31%
					Pl2-598-D3	PEPITO	108±11	4.9	n.m.	35.3	73	166	0.19	17.46	14.4	34.80%	35%
					Pl2-598-E1	PEPITO	121±8	4.86	n.m.	33.08	83	195	0.17	18.47	21.07	38.90%	39%
					Pl2-598-E2	PEPITO	133±8	4.71	n.m.	30.42	96	221	0.17	17.93	23.27	43.80%	43%
					Pl2-598-E3	PEPITO	154±8	4.69	n.m.	29.83	102	230	0.19	19.59	23.72	44.90%	50%
					M15FLU01	Ti-syringe	307	3.84	428	1.06	252	512	0.51	36.72	3.83	98.00%	/
					M15FLU02	Ti-syringe	307	4.21	431	4.31	234	509	0.54	33.98	3.49	92.00%	/
					M15FLU03	Ti-syringe	307	3.53	431	1.05	253	484	0.93	35.72	8.28	98.10%	/
					End-member		307		429±5	0	257±1	522±17	0,69±0,13	36,52±0,38	8,44±1,55		
					Missing fraction				/	0	/	/	/	6.5	-43.7		
White Castle	37°17.3576	32°16.8474	1709	2015	PL5-601-C1	PEPITO	93±23	5.38	n.m.	41.47	68.85	87.73	0.1	14.46	15.17	23.30%	29%
					PL5-601-	PEPITO	100±4	5.0	n.m.	33.8	122.3	147.84	0.36	16.61	19.86	37.40%	32%

					C2		3	6		6	5					
					PL5-601-C3	PEPITO	117±24	5.24	n.m.	38.57	91.15	110.61	0.33	14.82	18.16	28.70%	37%
					PL5-601-D1	PEPITO	113±27	5.2	n.m.	38.24	91.67	107.8	0.28	14.56	19.27	29.30%	36%
					M15FLU27	Ti-syringe	311	3.49	492	0.98	351.41	360.74	0.82	37.37	8.51	98.20%	/
					M15FLU26	Ti-syringe	311	3.81	488	4.05	330.23	385.57	1.1	35.68	6.27	92.50%	/
					M15FLU25	Ti-syringe	311	3.53	493	1.07	382.12	430.65	1.95	37.37	9.55	98.00%	/
					end-member				489±2	0	369±11	407±21	1,34±0.35	37,85±0,16	8,46±0,52		
					Missing fraction				/	0	/	/	/	11.32	-49.4		
Y3	37°17.512	32°16.671	1714	2014	PL7-582-B1	PEPITO	45±8	6.1	n.m.	35.82	28.52	50.48	0.27	n.m.	7.54	33.80%	14%
					PL7-582-B3	PEPITO	70±7	5.7	n.m.	37	50.58	98.96	0.36	n.m.	8.46	31.60%	21%
					PL7-582-C2	PEPITO	127±16	5.32	n.m.	33.48	88.88	172.72	0.27	n.m.	16.47	38.10%	39%
					M14FLU16	Ti-syringe	325	3.76	571	1.05	273.66	552.5	1.51	52.12	6.02	98.10%	
					M14FLU17	Ti-syringe	325	3.86	571	2.27	258	513.7	1.39	52.19	3.41	95.80%	
					M14FLU18	Ti-syringe	325	4.23	577	4.23	249.63	515.71	1.36	47.2	14.02	92.20%	
					end-member				574±2	0	273±3	553±9	1,49±0.03	52,50±1,08	8,07±3,47		
					Missing fraction				/	0	/	/	/	/	-24.9		

Capelinhos	37°17.3677	32°15.8298	1659	2015	PL6-602-D1	PEPITO	89±7	5.01	n.m.	38.33	107.57	512.16	0.13	11.11	8.54	29.20%	28%
					PL6-602-D2	PEPITO	101±4	4.97	n.m.	35.67	122.2	585.65	0.15	11.3	9.26	34.10%	31%
					PL6-602-D3	PEPITO	112±3	4.76	n.m.	34.72	159.94	741.36	0.14	12.61	10.16	35.80%	35%
					PL6-602-E1	PEPITO	131±4	4.75	n.m.	30.84	158.24	768.45	0.17	12.09	11.92	43.00%	38%
					PL6-602-E3	PEPITO	139±3	4.67	n.m.	30.88	197.14	857.34	0.23	12.49	11.69	42.90%	45%
					M15FLU37	Ti-syringe	318	3.28	273	1.27	597.64	2503.68	0.62	16.92	20.32	97.70%	/
					M15FLU38	Ti-syringe	318	3.2	274	1.54	543.72	2298.46	0.98	16.62	20.05	97.20%	/
					M15FLU39	Ti-syringe	318	3.21	276	1.39	589.27	2476.96	0.61	17.17	4.23	97.40%	/
					M15FLU40	Ti-syringe	318	3.19	275	1.4	584.34	2439.84	n.m.	16.77	29.13	97.40%	/
					end-member				268±2	0	594±12	2494±44	0,57±0.21	17,04±0,09	18,92±5,33		
					Missing fraction				/	0	/	/	/	2.03	-8.5		

Table 2

Site	Sample name	La pM	Ce pM	Pr pM	Nd pM	Sm pM	Eu pM	Gd pM	Tb pM	Dy pM	Ho pM	Er pM	Tm pM	Yb pM	Lu pM	∑DREE pM	DNd/DFe	La/La*	Eu/Eu*	Ce/Ce*	(La/Yb)N	143Nd/144Nd	±1sE	Dε Nd
NADW #		27.4	8.2	4.6	19.7	3.9	1	5.1	0.8	6	1.6	5.2	0.8	5.3	0.9	90.5								
Aisics	Pl2-598-D2	1041.7	992.4	126.1	478.7	72.6	138.3	73.5	10.6	57.5	9.4	22.4	2.5	12.3	1.6	3039.6	3.28E-6	1.14	8.07	3.99	16.41	n.m.	n.m.	n.d.
	Pl2-598-D3	2072.9	1363	179	672.5	100.2	188.2	98.3	13.9	76.1	12.7	29	3.1	15.3	1.8	4826.1	4.06E-6	1.58	8.06	3.83	26.39	0.512974	0.000013	6.6
	Pl2-598-E1	67.2	218	34.9	152.4	29.2	47.2	19.2	2.7	14.5	2.3	5.5	0.7	3.7	0.5	597.9	7.83E-7	0.34	8.07	3.6	3.57	0.513096	0.000010	8.9
	Pl2-598-E2	1196.6	1882.6	239.7	948.6	187.2	368.5	180.9	21.7	114.1	18.3	42.4	4.6	22.5	2.8	5230.5	4.30E-6	0.74	8.51	4.12	10.33	n.m.	n.m.	n.d.
	Pl2-598-E3	1269.4	2005.3	252	1004.5	196.3	392.3	191.1	23	119.8	19.2	44.5	4.9	24.2	3	5549.6	4.37E-6	0.75	8.61	4.21	10.21	0.513027	0.000008	7.6
	M15FLU01	2575.1	6849.2	705.3	2756.6	448.8	994.3	399.4	57.7	309.7	46.8	99.4	10.7	51.5	5.4	15309.9	5.38E-6	0.53	9.91	5.04	9.72	0.513097	0.000013	9.0
	End-member	2626.3	6987.3	719.5	2711.8	457.7	1014.4	407.3	58.9	315.8	47.7	101.2	10.9	52.4	5.5	15516.7	5.20E-6	0.5	9.91	4.9	9.74			
White Castle	PL5-601-C1	522.5	712.9	78.6	273.6	44	208.5	39.4	4.5	23.9	4.1	10.9	1.3	6.7	1	1931.9	3.12E-6	0.82	21.14	4.31	15.21	0.512986	0.000100	6.8
	PL5-601-C2	861.7	1115.4	124	437.9	61.8	283.8	57.3	7.1	37.4	6.3	15.6	1.9	9.5	1.3	3020.9	2.96E-6	0.87	20.19	4.32	17.61	0.513081	0.000007	8.6
	PL5-601-C3	687.6	866.6	96.2	327	42.7	206.2	40.9	5	27.4	4.7	11.5	1.4	7.4	1.1	2325.7	2.96E-6	0.86	20.94	4.22	18.17	0.513059	0.000004	8.2
	PL5-601-D1	683.2	851.2	93.8	314.2	38.9	186.1	36.3	4.7	25.5	4.3	11	1.3	6.6	1.1	2258.3	2.91E-6	0.86	20.98	4.2	19.97	0.513056	0.000013	8.2
	M15FLU27	3701	5325.6	563.7	2010	255.4	1205.9	229.1	30.7	152.8	23.6	49.3	5.3	26	3	13581.3	5.57E-6	0.83	21.04	4.57	27.63	0.513099	0.000086	9.0

	end-member	3770.2	5426.1	574.3	2047.5	260.2	1228.7	233.3	31.2	155.5	24	50.1	5.4	26.4	3	13835.9	3.92E-6	0.83	21.05	4.57	27.76			
Y3	PL7-582-B1	454.6	513.9	54.4	185.5	27.9	92.6	26.5	3.3	19	3.6	10	1.2	6.6	1	1400.3	3.67E-6	1.01	14.44	4.43	13.34	n.m.	n.m.	n.d.
	PL7-582-B3	681	765	80.5	262.4	29.9	88.8	27.8	3.8	22.2	4.4	11.7	1.4	7.4	1.1	1987.5	2.65E-6	0.97	13.05	4.33	17.88	n.m.	n.m.	n.d.
	PL7-582-C2	1044	1207.3	127	426.5	51.7	154.7	47.1	6.2	34.9	6.5	16.5	2.1	10.7	1.5	3136.5	2.47E-6	0.97	13.26	4.41	19.02	0.513031	0.000010	7.7
	M14FLU16	5512	6451.1	485.6	1710.4	207.9	709.7	182.2	23.7	125.5	21.1	47.9	5.1	25.1	3.1	15510.4	3.10E-6	1.42	15.36	6.37	42.67	0.513038	0.000005	7.8
	end-member	5622.5	6581.2	495.3	1744.5	212	724.1	185.7	24.2	127.9	21.5	48.7	5.2	25.4	3.1	15821.3	3.34E-6	1.42	15.37	6.37	43.03			
Capelinhos	PL6-602-D1	76.4	137.3	28.1	152.9	70	372.7	60.9	6.2	26.3	4.3	9.9	1.4	6.5	1.2	954.1	2.98E-7	1.03	24.02	3.8	2.3	n.m.	n.m.	n.d.
	PL6-602-D2	80.9	155.3	30.3	173.1	77.8	427.2	68	6.8	28.4	4	9.2	1	5.3	0.8	1067.9	2.96E-7	1.42	24.73	4.38	2.96	n.m.	n.m.	n.d.
	PL6-602-D3	102.6	201.7	28.5	100.6	19.2	87.2	14.6	2	7.1	0.8	1.3	0.1	0.4	0	566.2	1.36E-7	0.45	21.55	3.4	53.18	n.m.	n.m.	n.d.
	PL6-602-E1	97.8	196.3	37.8	210	78.6	426.3	70.8	8	34.3	5	11.7	1.4	7.3	1.2	1186.4	2.73E-7	1.11	24.14	4.2	2.59	n.m.	n.m.	n.d.
	PL6-602-E3	88.9	190	37.6	213	80.4	437.7	73	8.3	36	5	11.3	1.4	7	1	1190.4	2.48E-7	1.17	24.14	4.24	2.48	n.m.	n.m.	n.d.
	M15FLU37	1234	2340.1	238.2	1072.1	271	1648	289.6	33.1	161.6	32.8	74.9	12	70.7	11.1	7489	4.28E-7	0.98	25.16	5.85	3.39	0.513037	0.000009	7.8
	end-member	1269.8	2410.1	245.2	1103.6	279	1705.6	298.1	34.1	166.2	33.7	76.9	12.3	72.5	11.4	7718.5	2.11E-6	0.98	25.29	5.86	3.4			

Table 3

ppt	NADW	Aisics					White Castle					Capelinhos					Y3				
		End-member	Intercept	R^2	Missing REE	% DREE lost	End-member	Intercept	R^2	Missing REE	% DREE lost	End-member	Intercept	R^2	Missing REE	% DREE lost	End-member	Intercept	R^2	Missing REE	% DREE lost
La	3.8	357.7	422.1				514.1	274.4	0.87	239.7	46.6	171.4	25.7	0.94	145.7	85.0	765.6	370.3	0.99	395.3	51.6
Ce	1.15	959.7	570.8	0.97	388.9	40.5	746.2	359.8	0.86	386.4	51.8	327.9	63.1	0.97	264.8	80.7	903.9	436.0	0.99	467.9	51.8
Pr	0.65	99.4	72.2	0.97	27.2	27.3	79.4	39.1	0.85	40.3	50.8	33.6	11.8	0.98	21.8	64.9	68.4	45.2	0.99	23.2	33.9
Nd	2.84	397.6	291.2	0.96	106.4	26.8	289.9	136.1	0.82	153.9	53.1	154.6	69.3	0.99	85.3	55.2	246.7	153.7	0.99	93.0	37.7
Sm	0.58	67.5	57.5	0.88	10	14.8	38.4	18.7	0.73	19.7	51.2	40.8	29.2	0.93	11.5	28.3	31.3	18.7	0.97	12.6	40.2
Eu	0.16	151.1	115.9	0.88	35.2	23.3	183.2	94.7	0.79	88.5	48.3	250.4	165.3	0.94	85.1	34.0	107.8	58.8	0.92	49.0	45.5
Gd	0.8	62.8	58.2	0.89	4.6	7.3	36.0	17.9	0.74	18.1	50.3	45.5	27.0	0.95	18.5	40.7	28.6	17.4	0.96	11.2	39.2
Tb	0.13	9.2	7.2	0.94	2.0	21.6	4.9	2.2	0.74	2.7	55.1	5.3	3.0	0.98	2.3	43.9	3.8	2.3	0.98	1.5	38.8
Dy	0.98	50.3	38.1	0.95	12.2	24.3	24.8	11.5	0.74	13.3	53.7	26.3	12.3	0.99	14.0	53.1	20.4	12.9	0.99	7.5	36.7
Ho	0.26	7.7	6.1	0.95	1.6	20.5	3.9	1.8	0.70	2.1	53.3	5.4	1.6	0.94	3.8	70.5	3.5	2.3	0.99	1.1	33.0
Er	0.87	16.6	14.1	0.95	2.6	15.4	8.2	4.2	0.66	4.0	48.9	12.5	3.3	0.91	9.2	73.7	8.0	5.7	0.99	2.3	29.1
Tm	0.13	1.8	1.5	0.94	0.3	16.4	0.9	0.5	0.57	0.4	48.2	2.0	0.4	0.56	1.7	82.2	0.9	0.7	0.99	0.2	22.0
Yb	0.92	8.9	7.3	0.91	1.6	18.4	4.5	2.0	0.38	2.5	55.4	12.2	1.5	0.44	10.7	87.5	4.3	3.2	0.96	1.1	25.8

Lu	0.16	0.9	0.9	0.86	0.1	8.7	0.5	0.3	0.44	0.3	48.3	1.9	0.2	0.05	1.7	89.3	0.5	0.4	0.94	0.1	20.6
∑DREE		2191.3			592.6	27	1935.1			971.9	50.2	1089.9			676.1	62	2193.9			1066.1	48.6
La/La*		0.53			n.a.		0.83			0.81		0.98			0.95		1.42			2.51	
Ce/Ce*		5.04			7.34		4.57			4.81		5.85			6.23		6.37			10.55	
Eu/Eu*		9.91			19.52		21.04			19.99		25.16			25.25		15.36			17.53	

Table 4

		Aisics		**KD**	**White Castle**		**KD**	**Capelinhos**		**KD**	**Y3**		**KD**
	ppt	End-member	Missing REE		End-member	Missing REE		End-member	Missing REE		End-member	Missing REE	
La3+	La	357.7			514.1	239.7	0.47	171.4	145.7	0.85	765.6	395.3	0.52
Ce3+	Ce	959.7	388.9	0.41	746.2	386.4	0.52	327.9	264.8	0.81	903.9	467.9	0.52
Pr3+	Pr	99.4	27.2	0.27	79.4	40.3	0.51	33.6	21.8	0.65	68.4	23.2	0.34
Nd3+	Nd	397.6	106.4	0.27	289.9	153.9	0.53	154.6	85.3	0.55	246.7	93.0	0.38
Sm3+	Sm	67.5	10.0	0.15	38.4	19.7	0.51	40.8	11.5	0.28	31.3	12.6	0.4
Eu2+	Eu	151.1	35.2	0.23	183.2	88.5	0.48	250.4	85.1	0.34	107.8	49.0	0.45
Gd3+	Gd	62.8	4.6	0.07	36.0	18.1	0.5	45.5	18.5	0.41	28.6	11.2	0.39
Tb3+	Tb	9.2	2.0	0.22	4.9	2.7	0.55	5.3	2.3	0.44	3.8	1.5	0.39
Dy3+	Dy	50.3	12.2	0.24	24.8	13.3	0.54	26.3	14.0	0.53	20.4	7.5	0.37
Ho3+	Ho	7.7	1.6	0.2	3.9	2.1	0.53	5.4	3.8	0.7	3.5	1.1	0.33
Er3+	Er	16.6	2.6	0.15	8.2	4.0	0.49	12.5	9.2	0.74	8.0	2.3	0.29
Tm3+	Tm	1.8	0.3	0.16	0.9	0.4	0.48	2.0	1.7	0.82	0.9	0.2	0.22
Yb3+	Yb	8.9	1.6	0.18	4.5	2.5	0.55	12.2	10.7	0.87	4.3	1.1	0.26
Lu3+	Lu	0.9	0.1	0.09	0.5	0.3	0.48	1.9	1.7	0.89	0.5	0.1	0.21

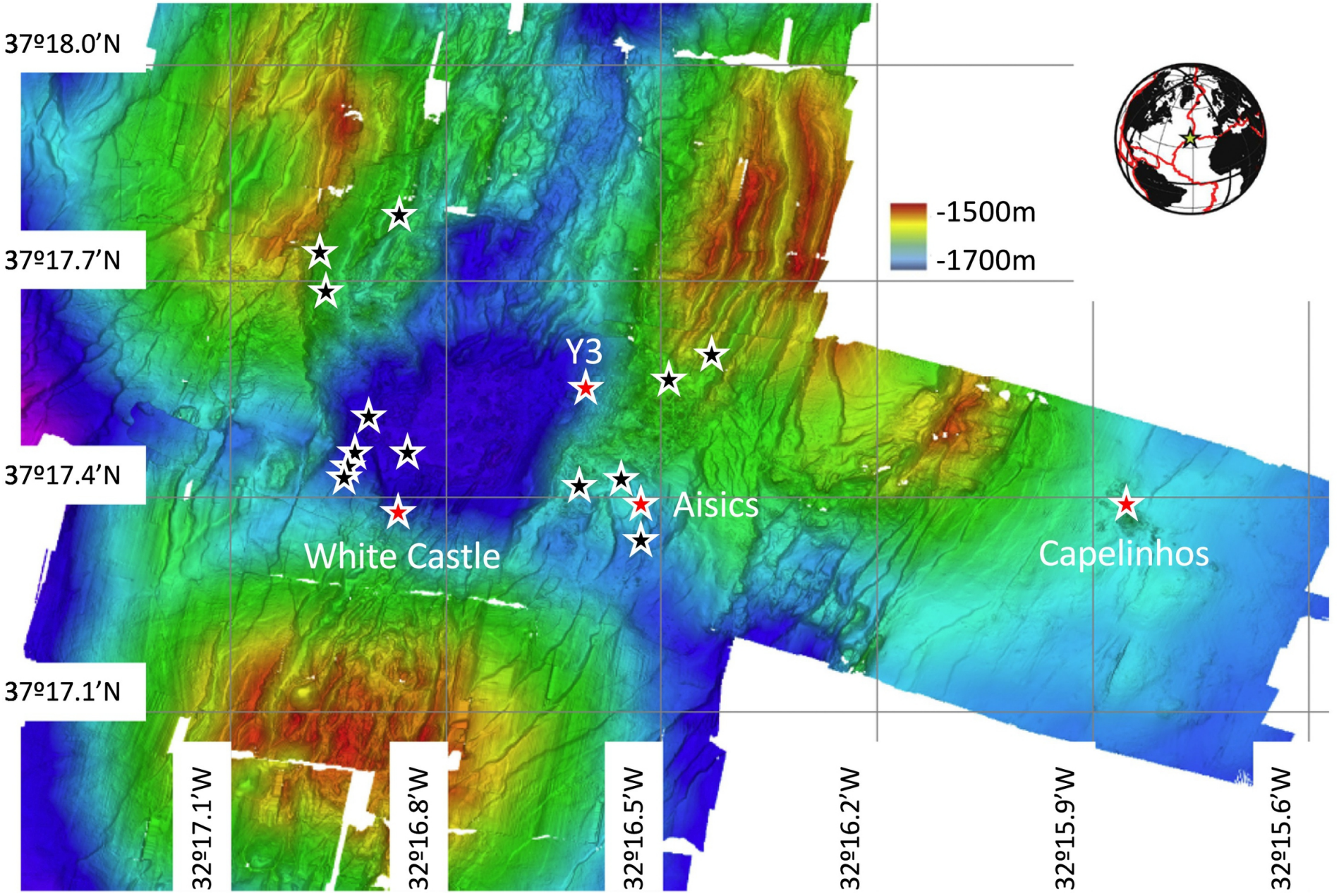
37º18.0'N
37º17.7'N
37º17.4'N
37º17.1'N
-1500m
-1700m
Y3
Aisics
White Castle
Capelinhos
32º17.1'W
32º16.8'W
32º16.5'W
32º16.2'W
32º15.9'W
32º15.6'W

Figure 1

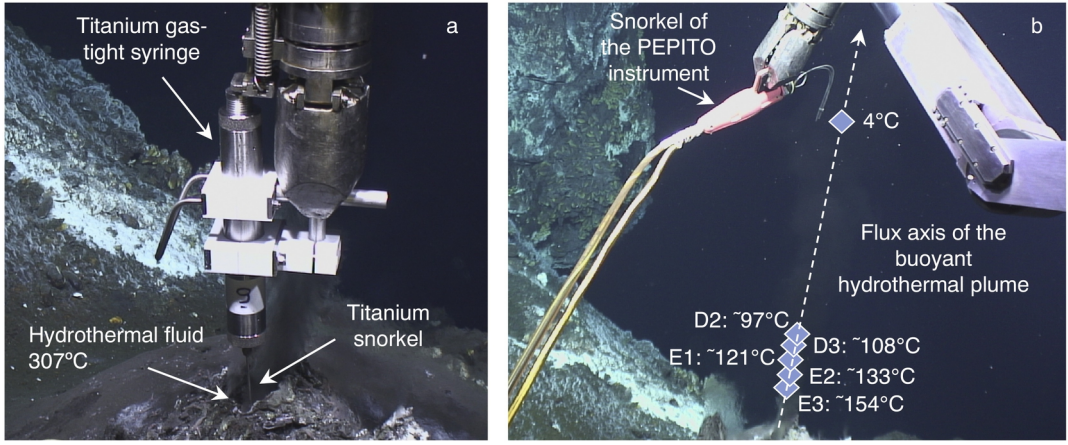
Titanium gas-tight syringe
a
Hydrothermal fluid 307°C
Titanium snorkel
Snorkel of the PEPITO instrument
b
4°C
Flux axis of the buoyant hydrothermal plume
D2: ~97°C
E1: ~121°C
D3: ~108°C
E2: ~133°C
E3: ~154°C

Figure 2

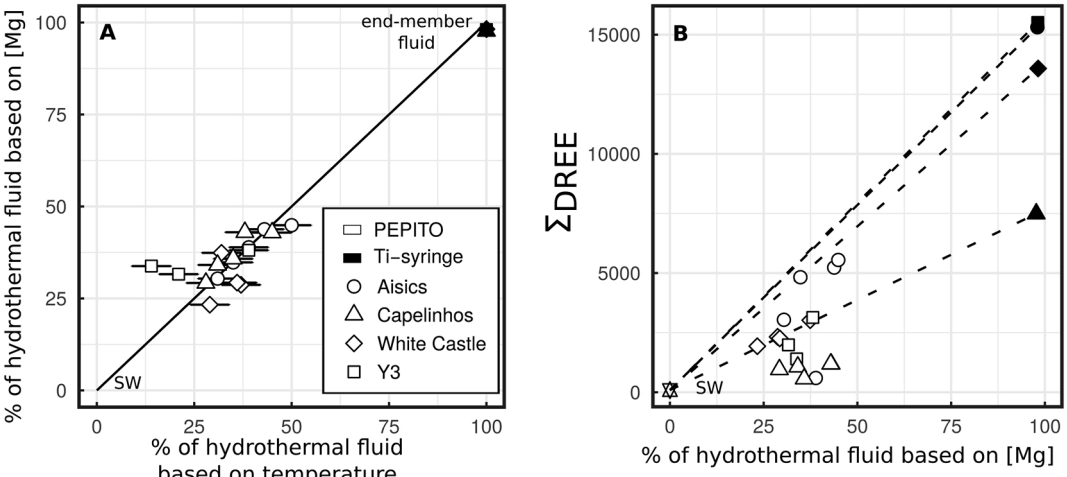
A
end-member fluid
SW
PEPITO
Ti–syringe
Aisics
Capelinhos
White Castle
Y3
% of hydrothermal fluid based on [Mg]
% of hydrothermal fluid based on temperature
0
25
50
75
100
B
ΣDREE
15000
10000
5000
SW
% of hydrothermal fluid based on [Mg]

Figure 3

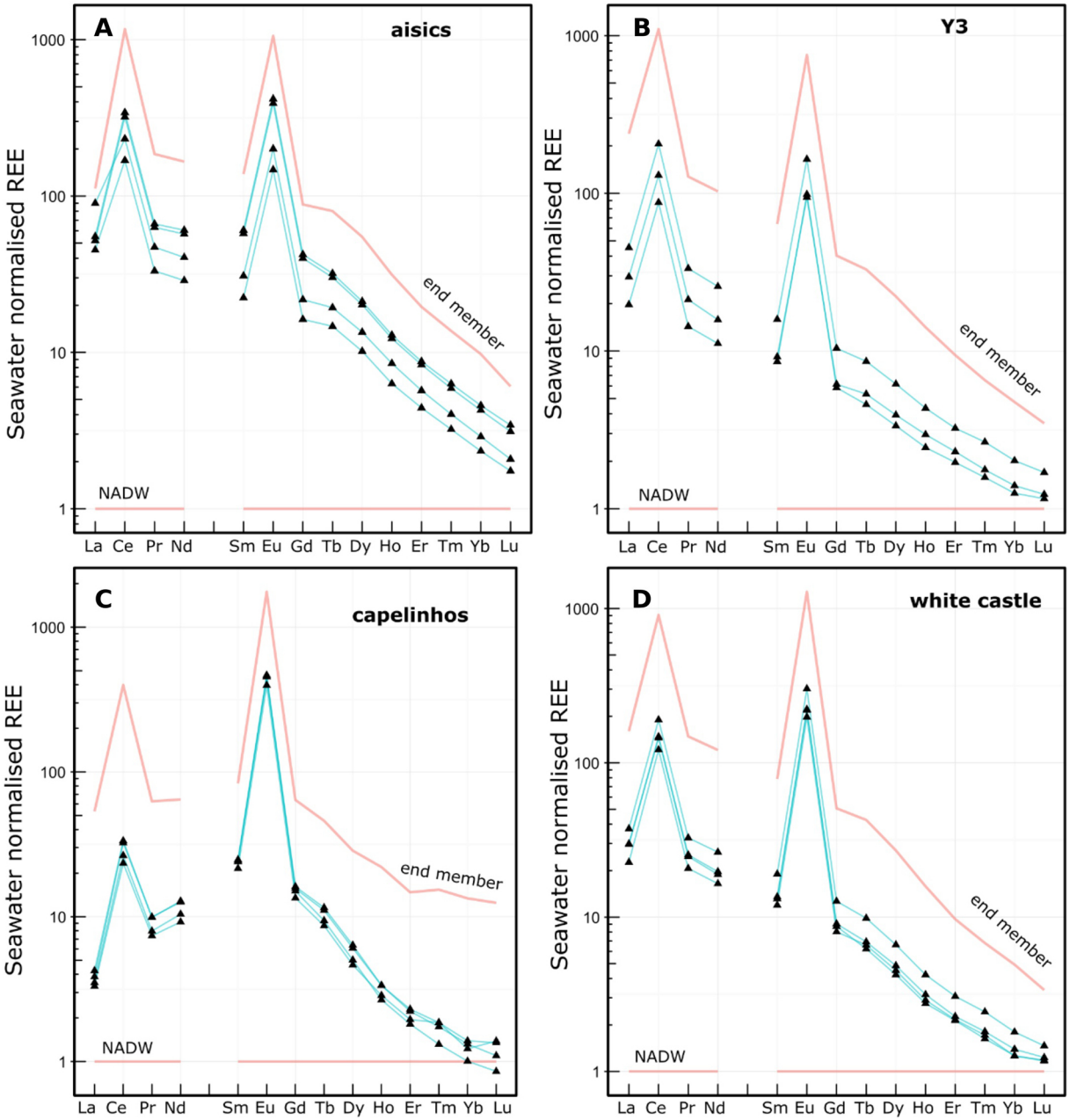
A
aisics
B
Y3
C
capelinhos
D
white castle
Seawater normalised REE
1000
100
10
1
end member
NADW
La Ce Pr Nd Sm Eu Gd Tb Dy Ho Er Tm Yb Lu

Figure 4

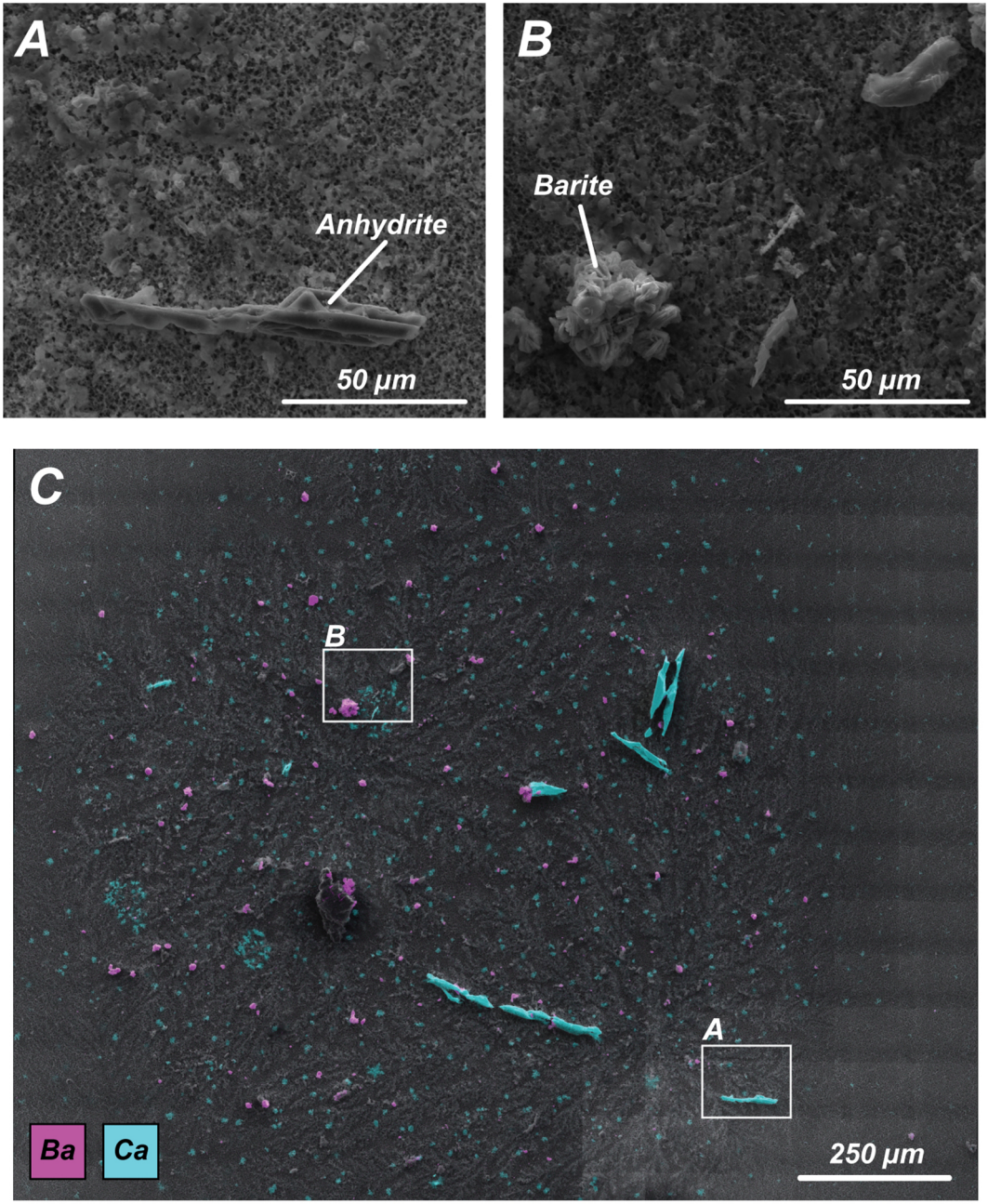

Figure 5

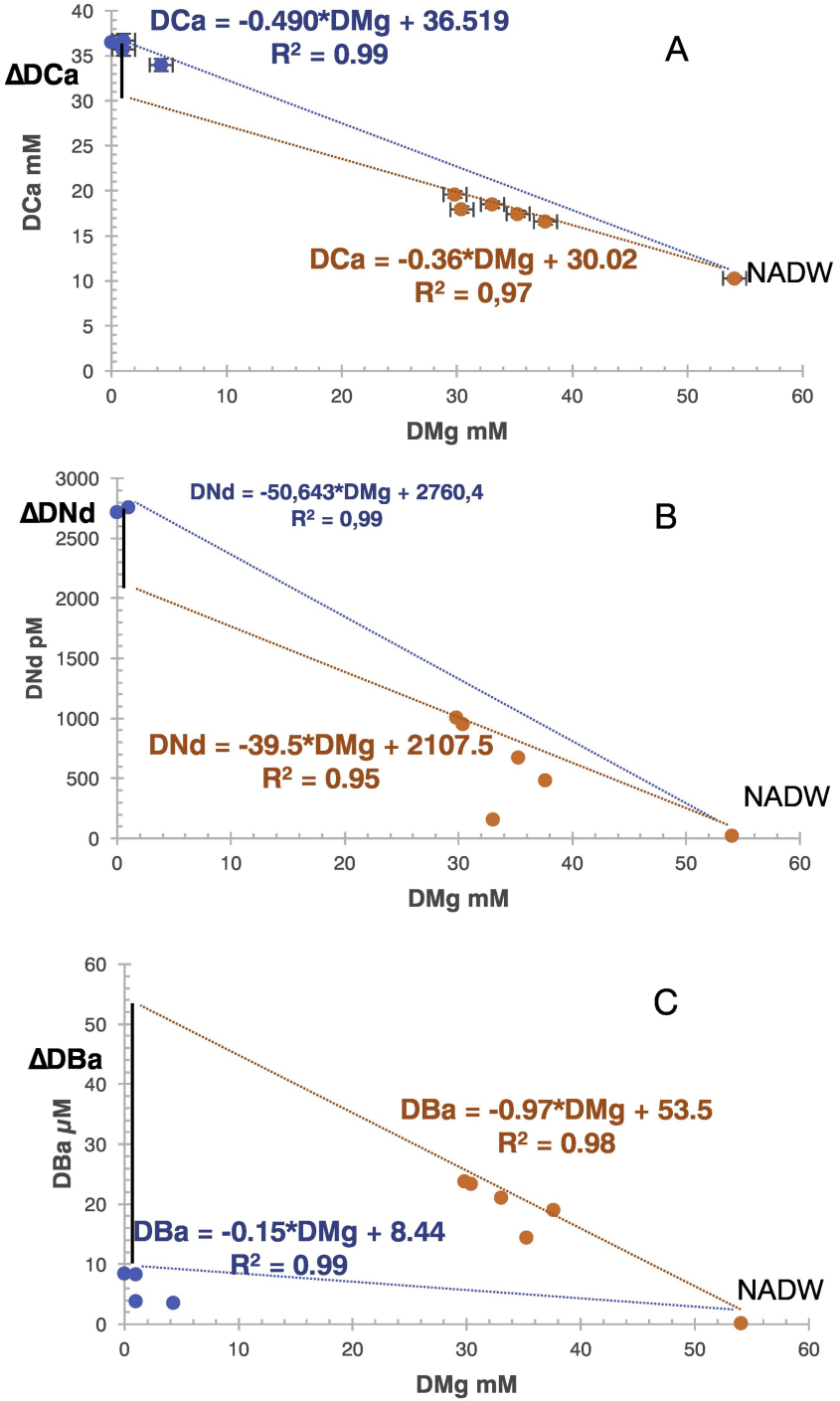
A
ΔDCa
DCa = -0.490*DMg + 36.519
R² = 0.99
DCa = -0.36*DMg + 30.02
R² = 0,97
NADW
DCa mM
DMg mM
B
ΔDNd
DNd = -50,643*DMg + 2760,4
R² = 0,99
DNd = -39.5*DMg + 2107.5
R² = 0.95
NADW
DNd pM
DMg mM
C
ΔDBa
DBa = -0.97*DMg + 53.5
R² = 0.98
DBa = -0.15*DMg + 8.44
R² = 0.99
NADW
DBa µM
DMg mM

Figure 6

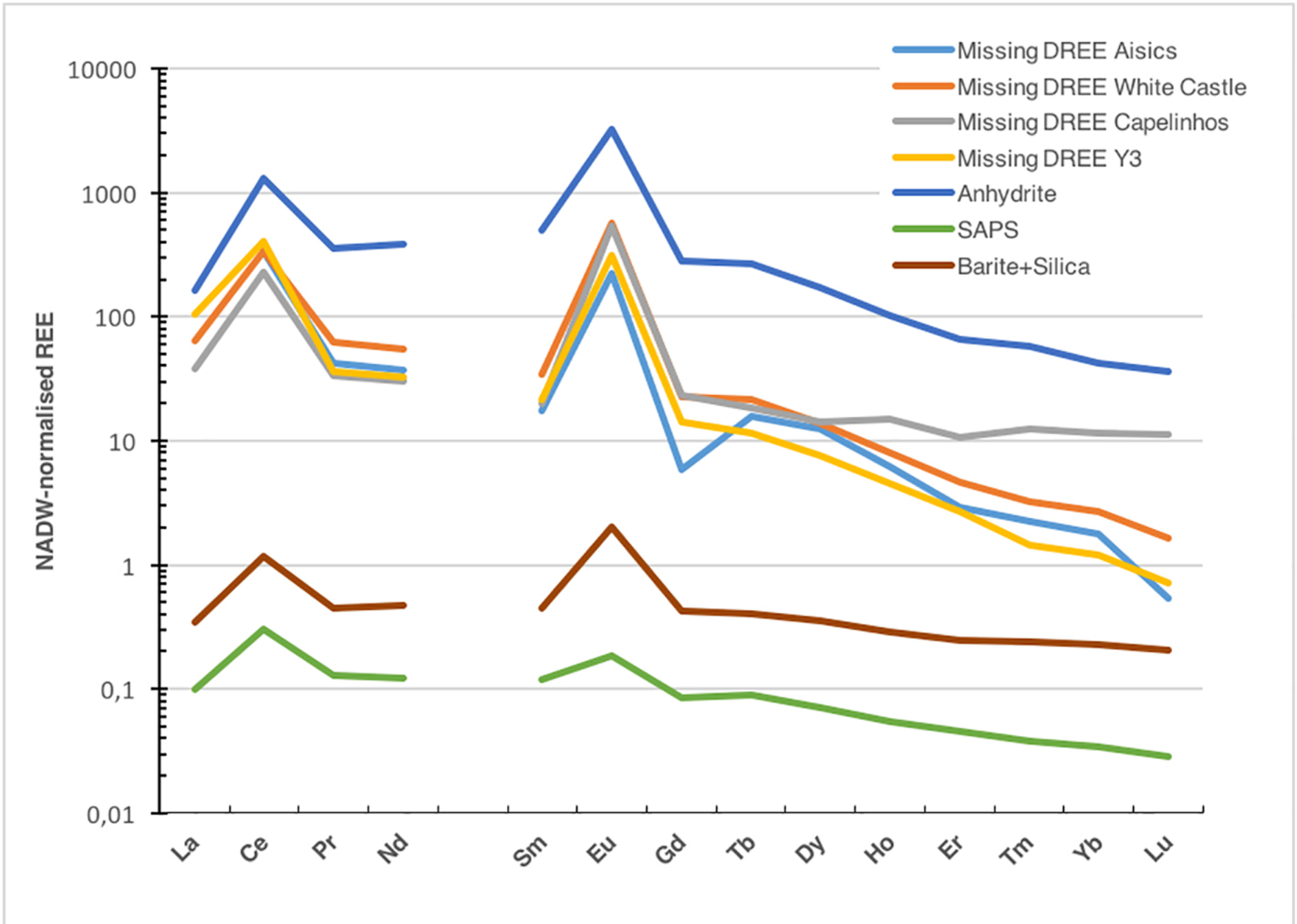
Missing DREE Aisics
Missing DREE White Castle
Missing DREE Capelinhos
Missing DREE Y3
Anhydrite
SAPS
Barite+Silica
NADW-normalised REE
10000
1000
100
10
1
0,1
0,01
La
Ce
Pr
Nd
Sm
Eu
Gd
Tb
Dy
Ho
Er
Tm
Yb
Lu

Figure 7

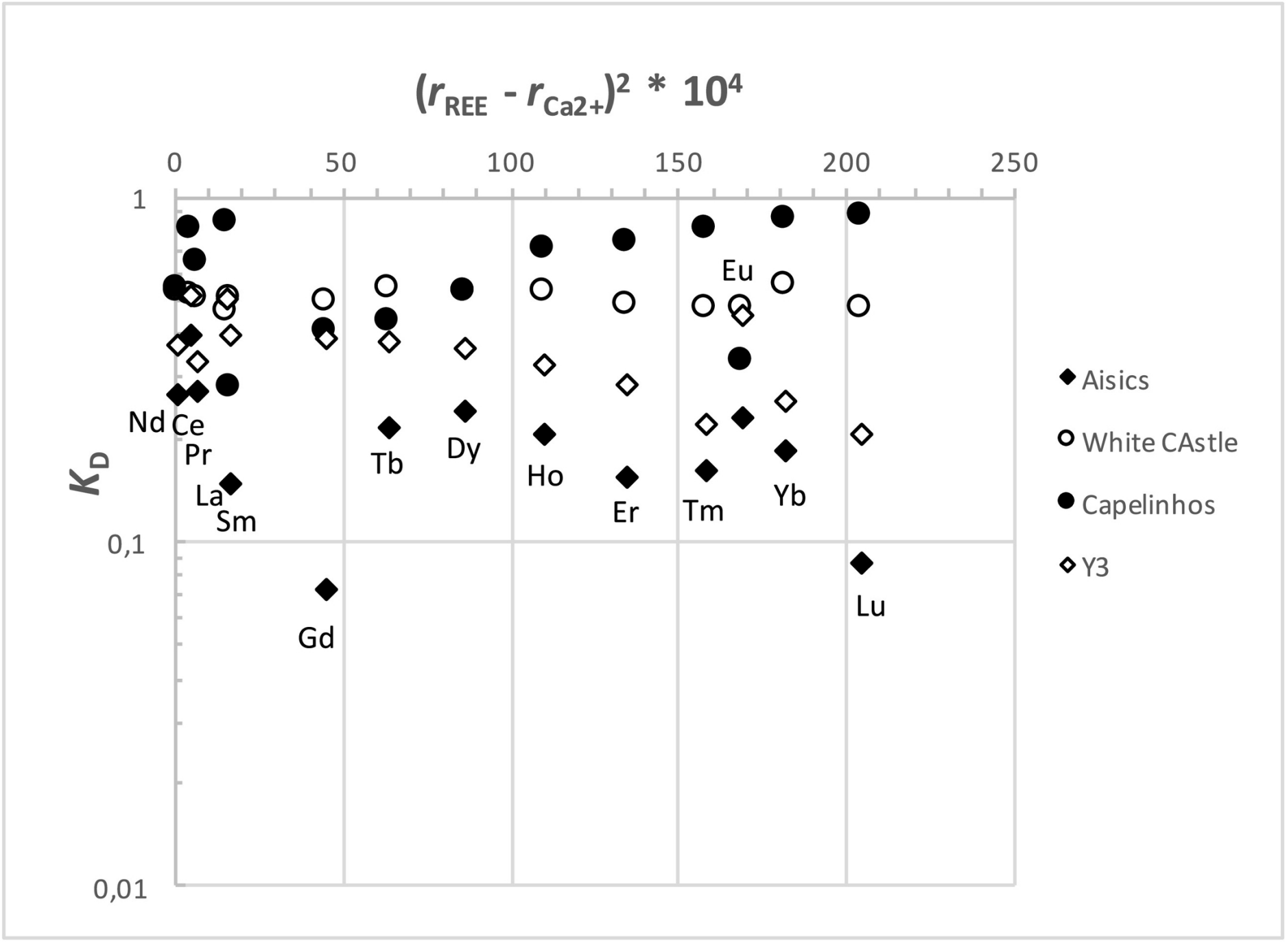
$(r_{REE} - r_{Ca2+})^2 * 10^4$
0
50
100
150
200
250
1
0,1
0,01
K_D
Nd
Ce
Pr
La
Sm
Gd
Tb
Dy
Ho
Er
Tm
Eu
Yb
Lu
Aisics
White CAstle
Capelinhos
Y3

Figure 8

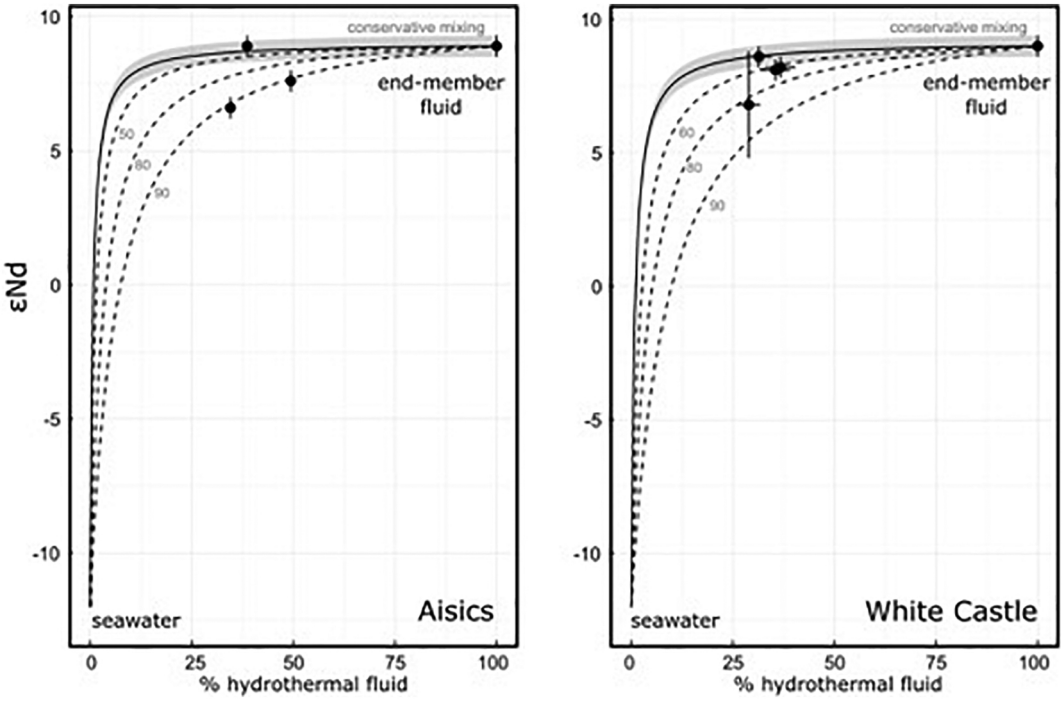
εNd
10
5
0
-5
-10
conservative mixing
end-member fluid
50
60
80
90
seawater
Aisics
0
25
50
75
100
% hydrothermal fluid
conservative mixing
end-member fluid
60
80
90
seawater
White Castle
% hydrothermal fluid

Figure 9